Petroleum Science 23 (2026) 4792–4809

Contents lists available at ScienceDirect

Petroleum Science

journal homepage: www.keaipublishing.com/en/journals/petroleum-science

Original Paper

Axial-torsional-lateral vibration model of drill bit considering axial and lateral cutting effects

Jin-Cheng Huang [a], Wen-Jun Huang [a,*], De-Li Gao [a,**], Wen-Tuo Li [b], Jin-Hui Zhou [a]

[a] MOE Key Laboratory of Petroleum Engineering, China University of Petroleum (Beijing), Beijing, 102249, China
[b] Hainan Branch of China National Offshore Oil Corporation Limited, Haikou, 570311, Hainan, China

A R T I C L E I N F O

Article history:
Received 26 March 2025
Received in revised form
1 December 2025
Accepted 1 April 2026
Available online 6 April 2026

Edited by Jia-Jia Fei

Keywords:
Tubular mechanics
Drill bit dynamics
Drill bit-rock interaction
Stick-slip vibration
Backward whirling

A B S T R A C T

In ultra-deep well drilling, the drill bit undergoes severe axial-torsional-lateral coupled vibrations, such as stick-slip and whirling, significantly increasing drilling risks. The evolution laws of these complex vibrations have not been fully revealed, making it challenging to design effective vibration mitigation strategies. Therefore, this paper aims to build a new drill bit dynamic model considering axial and lateral cutting processes to reveal the evolution laws of stick-slip and lateral vibrations. Firstly, by considering the three-dimensional cutting force while breaking rock, cutting limits, and nonlinear friction, the axial-lateral-torsional coupled vibration model of the drill bit was established. Next, the contact determination conditions between the drill bit and rock were extended, refining the three-dimensional bit-rock interaction model. Additionally, considering the complex time delay caused by axial-lateral-torsional vibrations, the realistic cutting profile for the drill bit was constructed. Consequently, the evaluation indexes for the stick-slip vibration and whirling of drill bit were developed. Finally, the validity of the model was confirmed through field data validation and comparison with the RGD model. The results indicate that the lateral motion of the drill bit undergoes a "collision-cutting-separation" process. The lateral alternating cutting motion intensifies stick-slip vibrations, reduces torsional amplitude stability, and raises the rotational speed threshold for escaping stick-slip vibration. As rotational speed increases, stick-slip vibration transitions to intermittent stick-slip vibration and eventually escapes from stick-slip vibration. The lateral cutting limit and torsional sticking state can lead to the lateral sticking state. With increasing rotational speed, the lateral motion changes from "collision-cutting-sticking-separation" to "collision-cutting-separation", with the lateral motion evolving from random backward motion to quasi-periodic backward motion and ultimately entering periodic backward whirling. This study provides a theoretical foundation for drilling parameter optimization and drill bit selection.

1. Introduction

Drilling engineering is critical in the geological exploration and extraction of oil and natural gas. A drilling system typically consists of a drilling rig, top drive system, and drill string, with the drill string as the primary carrier for energy transmission and rock breaking. The drill string comprises the upper drill string and the bottom hole assembly (BHA), the latter of which includes the drill bit, drill collar, stabilizers, and downhole measurement tools (Wang et al., 2025). During actual drilling operations, the drill string is usually lowered into a narrow wellbore, extending to several kilometers, and filled with a three-phase mixture of gas, liquid, and solid. The drilling bit is then driven forward through rotational motion and weight on bit (WOB), enabling the drilling of the well in the desired direction (Liu and Gao, 2017; Shi et al., 2021). However, the large length-to-diameter ratio characteristics of the drill string and the complex bit-rock interaction make the drill string system prone to self-excited vibration, which

* Corresponding author.
** Corresponding author.
E-mail addresses: huangwenjun1986@126.com (W.-J. Huang), gaodeli_team@126.com (D.-L. Gao).
Peer review under the responsibility of China University of Petroleum (Beijing).

https://doi.org/10.1016/j.petsci.2026.04.001

further evolves into lateral, axial, and torsional vibration (Khulief, 2025). The coupling between these vibrations may lead to more severe vibration modes, such as stick-slip vibration, bit bounce, and whirling (Li et al., 2022). Field data indicated that the time spent in stick-slip vibration in deep well drilling usually accounts for more than half of the total drilling time (Kriesels et al., 1999; Zhang et al., 2022). The alternating stresses induced by stick-slip vibration can significantly accelerate fatigue failure of the drill string and wear of the drill bit, thereby reducing drilling efficiency (Di et al., 2024). Therefore, an in-depth study of the mechanisms on stick-slip vibration occurrence and subsequent dynamic evolution behaviors is of great importance.

The studies on dynamic modeling of stick-slip vibration have gone through a staged development, from modeling torsional vibration alone to modeling coupled axial-torsional vibrations and then to modeling coupled axial-lateral-torsional vibrations. In early studies, researchers believed stick-slip vibration was solely related to torsional vibration (Luo et al., 2023). It was commonly assumed that the velocity-dependent weakening effect, in which the torque of bit (TOB) decreases as rotational speed increases, dominates the stick-slip vibration of the drill string (Gao and Huang, 2024; Shi et al., 2023). Based on this, several functional relationships were proposed to describe the dependence between the TOB and rotational speed (Choe et al., 2022; Liu et al., 2024). These models partially revealed the essential characteristics of the stick-slip vibration. However, with the validation of rock-breaking experiments and the deeper study of the mechanisms behind the stick-slip vibration, the velocity-dependent weakening assumption has proven challenging in explaining the experimental phenomenon accurately. It also fails to explain the intrinsic connection between stick-slip vibration and other vibration modes.

To overcome the limitations of the velocity-dependent weakening assumption, based on a large number of cutting experiments, Detournay and his team developed a bit-rock interaction model under the assumption of velocity independence (Detournay and Defourny, 1992; Detournay et al., 2008). This model was then applied to the two-degree-of-freedom drill string dynamics model (RGD model), achieving coupling of axial and torsional vibrations (Richard et al., 2004, 2007). The drill bit-rock interaction exhibits time-delay characteristics, meaning that the current cutting depth depends on the relationship between the current axial position and the axial position of the preceding cutter blade at the same angular displacement (Li et al., 2024a). Notably, the large length-to-diameter ratio of the drill string induces significant torsional vibration in the rotational motion, resulting in a non-constant time delay (state-dependent time delay) (Zhang and Detournay, 2020). The axial cutting depth can be obtained by solving the state-dependent delay differential equations (SDDDE). Subsequently, a series of scholars have made various improvements based on this model, including drill string discretization (Chen et al., 2021a; Xiang et al., 2023b; Zhang and Detournay, 2022), detailed bit modeling (Deng et al., 2024; Tian and Detournay, 2021; Tian et al., 2020; Zhang et al., 2024a), stability analysis (Bakhtiari-Nejad and Hosseinzadeh, 2017; Kumar et al., 2024), heterogeneous formations (Aribowo et al., 2022, 2023), drilling tool analysis (Aribowo et al., 2023; Dehkordi et al., 2022), modifications to the bit-rock interaction model (Zhang et al., 2024b), BHA structure optimization (Feng et al., 2019), and vibration control (Li et al., 2024b; Liu et al., 2021; Zheng et al., 2020), among others.

Due to the time delay characteristics of the drill bit-rock interaction and the influence of axial vibrations, the axial cutting depth is no longer controlled solely by the position of the previous cycle but also by multiple historical cycles (axial multiple regeneration effect) (Liu et al., 2020). When bit bounce occurs, the axial multiple regeneration effect becomes more pronounced. Although the RGD model can describe the stick-slip vibration characteristics, its drill bit-rock interaction model neglects the axial multiple regeneration effect, causing SDDDE to fail to capture the actual historical axial displacement, which leads to errors in axial cutting depth calculation (Hou et al., 2023). Liu Xianbo's studies increase computational accuracy by extending the historical search space of the SDDDE to account for axial multiple regeneration effects (Liu et al., 2023). Although this approach can partially increase computational accuracy, it significantly increases computational overhead. A two-dimensional diffusion equation was employed to characterize the functional relationship between angular and axial displacement to accurately calculate the axial cutting depth (Ambrus et al., 2024; Xie et al., 2023). Subsequently, the bottom-hole plane function was introduced by updating the functional relationship between angular and axial displacement in real time (Deng et al., 2021; Faghihi et al., 2024). These improved models consider the axial multiple regeneration effect and state-dependent time delay, further enhancing the computational accuracy. However, the models above only explain stick-slip vibration through the modeling of axial-torsional vibration and do not consider the influence of lateral vibration on stick-slip vibration, which cannot sufficiently reveal the evolution mechanisms of stick-slip vibration.

Currently, the lateral vibration is primarily addressed through Hertzian collision models in existing research (Cai et al., 2023; Liu et al., 2024; Xiang et al., 2023a). Unlike the contact between the drill string and the wellbore, the contact between the bit and the rock involves lateral and axial cutting motions, and thus, it is influenced by the axial and lateral multiple regeneration effect and state-dependent time delay. Therefore, it is difficult to use the Hertzian contact model to accurately obtain the three-dimensional force on the drill bit and reveal the evolution mechanisms of stick-slip vibrations. Liu Xianbo developed a three-dimensional drill bit-rock interaction model and revealed the influence of lateral cutting on stick-slip vibration (Liu et al., 2013). However, this study still has certain limitations in calculating the axial and lateral cutting depths and the three-dimensional bit-rock interaction model.

In this paper, a drill bit time-delay dynamics model (DBTD) based on axial-torsional-lateral coupled vibrations is built. The key to the DBTD model is the three-dimensional bit-rock interaction model, in which the multiple regeneration effects caused by axial and lateral vibrations and state-dependent time delay due to torsional vibration are considered. The axial cutting profile function and lateral cutting trajectory function are adopted to calculate the axial and lateral cutting depths. The validity of the DBTD model is demonstrated through field data validation and comparison with the RGD model. At last, the three-dimensional force characteristics of the drill bit and the evolution mechanisms of stick-slip vibration and lateral motion are explored.

2. Drill bit dynamics model

2.1. Four-degree-of-freedom dynamic equations

To simplify the system, the following assumptions are made in this study.

(1) The drill string is equivalent to a single mass, and both axial and torsional damping and stiffness are proportional to the length of the drill string.
(2) The drill bit is simplified into a rigid, planar multi-blade assembly with uniformly distributed blades, a constant wear flat length, and a maximum cutting limit.
(3) The drillability of the formation is isotropic.

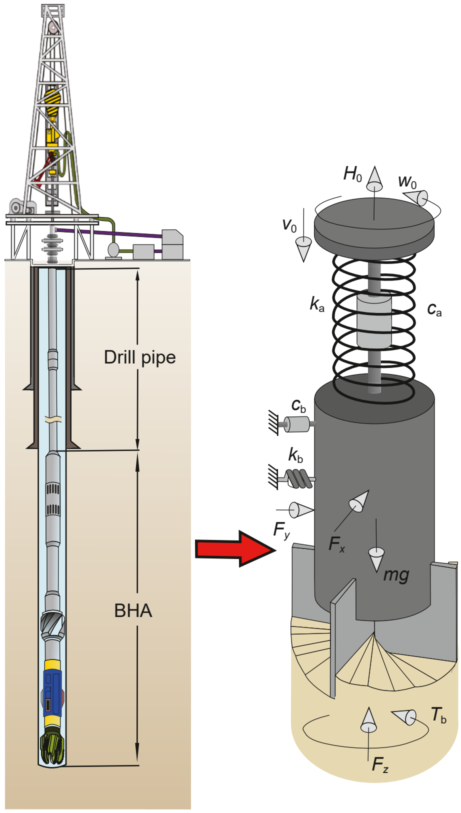

Fig. 1. Drilling system and equivalent model.

(4) The drill bit-rock interaction can be decomposed into two independent components: friction and cutting.
(5) The coupling between axial and lateral vibrations in the computation of the axial and lateral cutting depth is neglected.

This model expands the two-degree-of-freedom RGD model (Richard et al., 2004, 2007) to characterize lateral-axial-torsional vibrations, as shown in Fig. 1.

Two coordinate systems are defined based on the right-hand rule. The first is a fixed coordinate system (*O-XYZ*), in which the positive *Z*-axis is aligned with the axial direction of the drill bit, and the positive *X*-axis points in a direction perpendicular to the *Z*-axis. The second is a follower coordinate system (O_1-$X_1Y_1Z_1$), whose origin translates with the bit center at the current time step while its axes remain fixed relative to the global coordinate frame—that is, it does not rotate with the bit angle. The dynamic boundary conditions are established by the constant rotational speed ω_0 and hook running speed v_0. The lower boundary of the model is defined by the three-dimensional bit-rock interaction model and the initial weight of bit W_0. From the perspectives of system kinetic and potential energy, four-degree-of-freedom dynamic equations are constructed based on the Lagrangian equation, resulting in a set of four-degree-of-freedom equations, as shown in Eq. (1).

$$
\begin{aligned}
& m\ddot{x} + c_b\dot{x} + k_b x = -F_x \\
& m\ddot{y} + c_b\dot{y} + k_b y = -F_y \\
& m\ddot{z} + c_a(\dot{z} - v_0) + k_a(z - v_0 t) = W_0 - F_z \\
& J\ddot{\theta} + c_t(\dot{\theta} - \omega_0) + k_t(\theta - \omega_0 t) = -T_b
\end{aligned}
\tag{1}
$$

where m is the equivalent mass of the drill string, kg; J is the equivalent moment of inertia, kg/m^2; k_a is the equivalent axial stiffness, N/m; k_b is the equivalent lateral stiffness, N/m; k_t is the equivalent torsional stiffness, (N·m)/rad; c_a is the equivalent axial damping, (N·s)/m; c_b is the equivalent lateral damping, (N·s)/m; c_t is the equivalent torsional damping, (N·s·m)/rad; F_x is the *X*-direction force on drill bit, N; F_y is the *Y*-direction force on drill bit, N; F_z is the *Z*-direction force on drill bit, N; T_b is the torque on drill bit, N·m; W_0 is the weigh on drill bit, N.

2.2. Three-dimensional bit-rock interaction model

In the calculation of drill bit-rock interaction, accounting for the complex geometrical features of a PDC drill bit-such as cutter tip arcs, back reamer cavities, and tooth profiles—substantially increases the degrees of freedom in the dynamic model and the computational cost of the numerical solution. Therefore, the PDC drill bit's blades and tooth arrangement are idealized as rigid planar surfaces (Detournay et al., 2008). Based on this geometric simplification, the rock-breaking process is decomposed into a cutting force F_c and a friction force F_f (Detournay and Defourny, 1992), as illustrated in Fig. 2, by computing the planar blade cutting depth d_{ai}. This approach significantly reduces computational complexity while accurately capturing the dynamic interaction characteristics between the drill bit and rock. Compared with the 2D model (Liu et al., 2013), lateral forces induced by axial cutting, cutting limits of cutter blades and nonlinear friction factors were further considered in the 3D bit-rock interaction model.

The forces in the *z*-direction are primarily those generated by the axial cutting and friction, as shown in Eq. (2).

$$
F_z = \sum_{i=1}^{N} \zeta \varepsilon r H(\dot{\theta}) R(d_{ai}) + r l_{ai} \sigma H(\dot{z}) H(d_{ai}) + F_{aci} \tag{2}
$$

where ε is the intrinsic specific energy of rock, MPa; σ is the contact strength of rock, MPa; ζ is the cutter face inclination; r is the radius of the drill bit, mm; l_{ai} is the effective axial friction surface width of the *i*-th cutter blade, mm; d_{ai} is the axial cutting depth of the *i*-th cutter blade, mm; N is the number of cutter blades on the drill bit; $H(x)$ is the Heaviside function; $R(x)$ is the Ramp function; F_{aci} is the axial rigid body collision force of the *i*-th cutter blade, N.

To effectively simulate the friction forces during actual rock cutting, the effective widths of the axial and lateral friction surfaces are determined by Eq. (3) below (Detournay et al., 2008).

$$
l_{a/li} = \begin{cases} l_{a/lm} & \kappa d_{a/li} \geq l_{a/lm} \\ \kappa d_{a/li} & \kappa d_{a/li} < l_{a/lm} \end{cases} \tag{3}
$$

where l_{am} is the maximum axial wearflat length of the drill bit, mm; l_{lm} is the maximum lateral wearflat length of the drill bit, mm; κ is the wearflat coefficient; l_{li} is the effective lateral friction

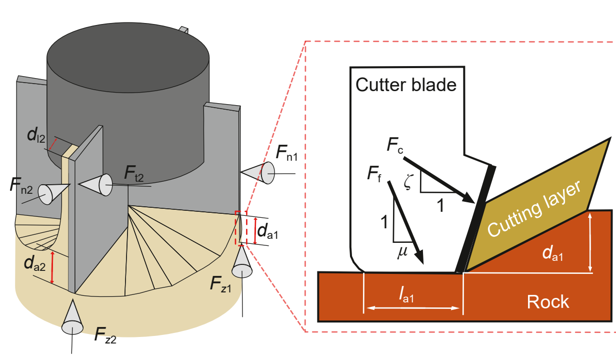

Fig. 2. Forces in the rock-cutting process.

surface width of the i-th cutter blade, mm; d_{li} is the lateral cutting depth of the i-th cutter blade, mm. Lateral forces are generated both by axial cutting & friction and lateral cutting & friction. Lateral forces are determined by superimposing the normal and tangential forces of each cutter blade through coordinate transformations. The normal and tangential components of lateral forces are calculated with Eq. (4).

$$\begin{aligned}&F_{ni}=\zeta\varepsilon bd_{li}H(r\dot{\theta}+v_{ti})R(d_{li})H(\dot{\theta})+bl_{li}\sigma H(v_{ni})H(d_{li})+F_{lci}\\&F_{ti}=\varepsilon bd_{li}H(r\dot{\theta}+v_{ti})R(d_{li})H(\dot{\theta})+\gamma\mu\sigma l_{li}bH(v_{ni})H(d_{li})\mathrm{sign}(r\dot{\theta}+v_{ti})+\\&\varepsilon rd_{ai}R(d_{ai})H(\dot{\theta})+\gamma\mu\sigma l_{ai}rH(\dot{z})H(d_{ai})\mathrm{sign}(\dot{\theta})\end{aligned}\tag{4}$$

where F_{lci} is the lateral rigid body collision force of the i-th cutter blade, N; F_{ni} is the normal force on the i-th cutter blade, N; F_{ti} is the tangential force on the i-th cutter blade, N; sign(x) is the sign function; b is the height of drill bit, mm; v_{ni} is the normal velocity of the i-th cutter blade, m/s; v_{ti} is the tangential velocity of the i-th cutter blade, m/s; γ is the geometric parameters of drill bit; μ is the coefficient of friction. The components of lateral forces along the x and y directions for each cutter blade can be calculated with the following equation:

$$\begin{bmatrix}F_{xi}\\F_{yi}\end{bmatrix}=\begin{bmatrix}\cos\Phi_i & -\sin\Phi_i\\ \sin\Phi_i & \cos\Phi_i\end{bmatrix}\begin{bmatrix}F_{ni}\\F_{ti}\end{bmatrix}\tag{5}$$

where F_{xi} is the X-direction force of the i-th cutter blade, N; F_{yi} is the Y-direction force of the i-th cutter blade, N; Φ_i is the angular displacement of the i-th cutter blade, rad. The angular displacement of each cutter blade is calculated as shown in Eq. (6).

$$\Phi_i=\mathrm{Rem}(\theta+\theta_i,2\pi),\quad i=1,2,\dots,N\tag{6}$$

where θ_i is the angle between each blade and the first blade, rad; Rem(·) is the remainder function. Then, the components of the total lateral forces on the drill bit along the x and y directions can be obtained from Eq. (7).

$$F_x=\sum_{i=1}^{N}F_{xi},\quad F_y=\sum_{i=1}^{N}F_{yi}\tag{7}$$

The torque on the drill bit is generated by the lateral and axial contacts of the drill bit and rock, as shown in Eq. (8).

$$T_b=\sum_{i=1}^{N}\begin{matrix}0.5\varepsilon r^2H(d_{ai})R(\dot{\theta})+0.5\gamma\mu\sigma l_{ai}r^2H(\dot{z})H(d_{ai})\mathrm{sign}(\dot{\theta})+\\ rb\varepsilon d_{li}H(r\dot{\theta}+v_{ti})H(\dot{\theta})R(d_{li})+rb\gamma\mu l_{li}\sigma H(v_{ni})\mathrm{sign}(r\dot{\theta}+v_{ti})H(d_{li})\end{matrix}\tag{8}$$

As shown in Eqs. (2)–(8), it is evident that the forces and torques acting on the drill bit are combinations of non-smooth functions of axial and lateral cutting depths, axial and lateral wearflat lengths, angular velocity, axial speed, and normal and tangential speeds of each blade.

To keep the simulated cutting behaviour physically realistic, the axial and lateral cutting depths are constrained by the maximum axial and radial exposures of the cutters, respectively. The detailed motivation, supporting literature and parameter selection are provided in Appendix A. When the axial cutting depth d_{ai} or the lateral cutting depth d_{li} reaches the maximum axial and lateral cutting depth $d_{a/lc}$, cutting and rigid-body collision are assumed to coexist. The rigid contact behavior is enforced using a penalty-based collision formulation: a penalty stiffness k_p generates a contact force to restrict any excess penetration beyond $d_{a/lc}$, while the additional penetration is not used to update the bottom-hole profile or cutting forces. In this way, the drill bit remains effectively rigid, and the enforcement of the depth constraint does not introduce elastic degrees of freedom into the system. The collision force F_c is calculated as:

$$F_{a/lci}=\begin{cases}k_p\left(d_{a/li}-d_{a/lc}\right) & d_{a/li}-d_{a/lc}>0\\ 0 & d_{a/li}-d_{a/lc}\le 0\end{cases}\tag{9}$$

where $d_{a/lc}$ is the corresponding axial and lateral limits imposed by the cutter exposures, mm; k_p is the equivalent lateral collision stiffness, N/m. The bit-rock interaction state is determined using a series of functions, including the Heaviside function, the Ramp function, and the sign function. To assess the axial state of the bit-rock interaction, several parameters are considered, including axial cutting depth d_{ai}, axial speed $\dot{z}$, and angular speed $\dot{\theta}$ (Liu et al., 2020). For the lateral state of bit-rock interaction, the relevant parameters include lateral cutting depth d_{li}, normal speed of the cutter blade v_{ni}, and tangential speed v_{ti}. The classification of bit-rock interaction is shown in Table 1.

2.3. Calculation method of cutting depth

In the three-dimensional bit-rock interaction model, the axial and lateral cutting depths of each cutter blade are essential for calculating the axial and lateral forces on the drill bit. To calculate the lateral and axial cutting depths, it is necessary to consider the

Table 1
Classification of bit-rock interaction.

Parameters			States
$d_{ai}\ge 0$	$\dot{z}\ge 0$	$\dot{\theta}\ge 0$	Axial cutting and friction
	$\dot{z}<0$	$\dot{\theta}\ge 0$	Axial cutting
	$\dot{z}\ge 0$	$\dot{\theta}<0$	Reversed friction force/torque
	$\dot{z}<0$	$\dot{\theta}<0$	No cutting and friction
$d_{ai}<0$	-	-	No contact with rock
$d_{li}\ge 0$	$v_{ni}\ge 0$	$r\dot{\theta}+v_{ti}\ge 0$	Lateral cutting and friction on i-th cutter blade
	$v_{ni}<0$	$r\dot{\theta}+v_{ti}\ge 0$	Lateral cutting without friction on i-th cutter blade
	$v_{ni}\ge 0$	$r\dot{\theta}+v_{ti}<0$	Reversed friction force without cutting on i-th cutter blade
	$v_{ni}<0$	$r\dot{\theta}+v_{ti}<0$	There is no cutting and friction on i-th cutter blade
$d_{li}<0$	-	-	There is no cutting and friction on i-th cutter blade

historical cutting displacements generated in the previous cutting process. However, due to the multiple regeneration effects and state-dependent time delays inherent in the cutting process, the rock profile created by the drill bit is not solely determined by the historical displacement of the previous cutter blade. Instead, it is influenced by the historical displacements of multiple cutter blade delay cycles. This characteristic leads to the existence of multiple solutions. To solve this problem, the axial cutting profile function and lateral cutting trajectory function are introduced to determine the actual historical cutting displacement of each cutter blade.

2.3.1. Calculation method of axial cutting depth

In the computation of the axial cutting depth, the influence of the lateral vibration is neglected so that the axial cutting behavior depends solely on the axial displacement and angular position of the drill bit. Based on the global coordinate system, the axial cutting profile function $U(\Phi_i)$ is constructed to characterize the relationship between the axial historical trajectory and angular displacement of the drill bit, as shown in Eq. (10).

$$U(\Phi_i) = \max(z(t), U(\Phi_i)), \quad i = 1, 2, \ldots, N \tag{10}$$

where $U(\Phi_i)$ is the axial cutting profile function, mm. Therefore, when the i-th cutter blade is engaged in cutting, the axial cutting depth depends on the difference between the current axial displacement and the historical axial cutting displacement corresponding to the current angular displacement in the axial cutting profile function, as expressed in Eq. (11).

$$d_{ai} = z(t) - U(\Phi_i) \tag{11}$$

When the i-th cutter blade is engaged in cutting, the corresponding axial cutting profile function is updated based on the current cutting displacement. If the i-th cutter blade is not engaged in cutting, the axial cutting depth is set to zero, and the axial cutting profile function remains unchanged. Following these updating rules, the profile function effectively eliminates the false displacements caused by the axial multiple regeneration effect, ensuring the accuracy of the axial cutting depth calculation. As illustrated in Fig. 3, the axial cutting depth d_{a4} of the fourth cutter blade is determined by the current and historical cutting displacements of the third cutter blade. The historical displacement of the third cutter blade is obtained from the axial cutting profile function.

2.3.2. Calculation method of lateral cutting depth

The lateral cutting depth of each cutter blade depends on the interaction between the instantaneous cutter position and the previously cut rock surface. Since lateral motion, rotation, and axial motion of the drill bit jointly contribute to the formation of a fully three-dimensional cutting profile, a direct computation of the true geometric intersection would be prohibitively expensive. In this study, the influence of axial displacement on the lateral cutting depth is neglected. Accordingly, the three-dimensional cutting profile is reduced to a two-dimensional cutting profile, from which it follows that the evaluation of the lateral cutting depth is determined solely by the lateral displacement and the angular position of the drill bit.

To represent the lateral cutting profile, a discrete lateral trajectory dataset is constructed for each cutter blade. The dataset collects the lateral coordinates of a blade in the global coordinate over its cutting history, and its definition is given in Eq. (12).

$$\chi_j(t') = \left\{ [x(t') + r\cos\theta(t'), y(t') + r\sin\theta(t')] \,\middle|\, \theta(t') \geq \theta(t) - \frac{2s\pi}{N} \right\}, \quad j = 1, \ldots, N \tag{12}$$

where t' denotes historical time, $\chi_j(t')$ is historical lateral trajectory dataset of cutter blade j in the global coordinate, N is the number of blades, $x(t')$ and $y(t')$ are the historical lateral displacement of the drill bit center in the global coordinate frame, $\theta(t')$ and $\theta(t)$ are the historical and current angular displacements, respectively, and s is the regeneration-order parameter. The angular constraint $\theta(t') \geq \theta(t) - 2s\pi/N$ ensures that only the portion of the previously cut surface relevant to the current blade position is retained. The necessity of introducing this regeneration-based indexing becomes apparent upon examining the computational requirements. For a drill bit with four blades ($N = 4$), rotating at 60 r/min, with a mechanical ROP of 18 m/h and a bit radius of 0.1 m, a 0.1 m drilling

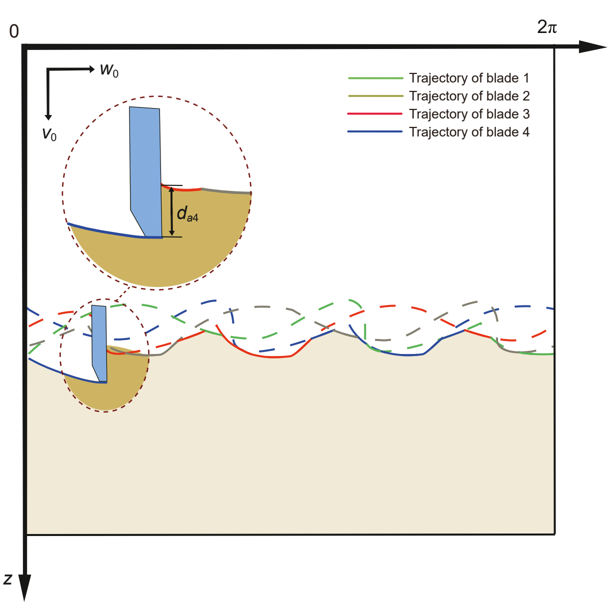

Fig. 3. Calculation of axial cutting depth while considering axial multiple regeneration effect.

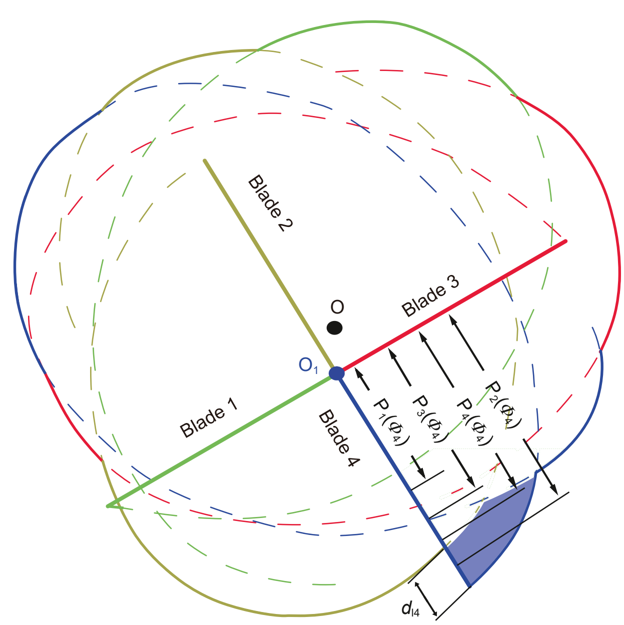

Fig. 4. Calculation of lateral cutting depth while considering lateral multiple regeneration effect.

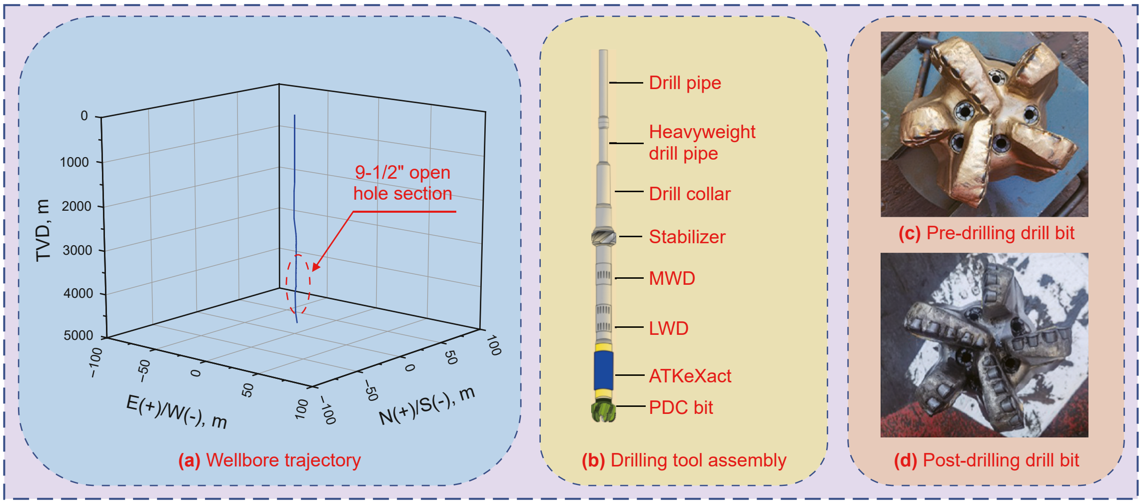

Fig. 5. Field description of the full hole section. (**a**) 3D wellbore trajectory illustrating the spatial profile of the entire section. (**b**) Drilling tool assembly used in this full 9-1/2″ hole section (4035–5079.3 m). (**c**) Drill bit condition before drilling. (**d**) Drill bit condition after drilling, indicating cutter wear and structural damage.

interval yields approximately 400,000 trajectory samples at a time resolution of 0.0002 s. Performing reconstruction over such a dataset at every time step would be computationally prohibitive. By applying a finite regeneration-order constraint of $s = 12$, the angular indexing limit is reduced to $2s\pi/N$, and only trajectories cut within this angular range are retained, reducing the total number of historical points to approximately 60,000. This corresponds to an 85% reduction in indexing cost while retaining the essential regeneration effect required for accurate cutting depth evaluation.

To calculate the lateral cutting depth, the historical lateral trajectory $\chi_j(t')$ is first transformed from the global coordinate system into the follower coordinate system at the current time step. The follower frame translates with the bit but does not rotate with $\theta(t)$, ensuring geometric consistency. The coordinate transformation is given by:

$$\begin{aligned}\tilde{x}_j &= x(t') + r\cos\theta(t') - x(t)\\ \tilde{y}_j &= y(t') + r\sin\theta(t') - y(t)\end{aligned} \tag{13}$$

where $\tilde{x}_j, \tilde{y}_j$ denote the historical lateral displacement expressed in the follower coordinate system at the current time step, transformed from the global coordinate frame. Each transformed trajectory point is then expressed in polar coordinates:

$$\rho_j = \sqrt{\tilde{x}_j^2 + \tilde{y}_j^2},\ \ \Phi_j = \tan^{-1}\left(\frac{\tilde{y}_j}{\tilde{x}_j}\right) \tag{14}$$

where ρ_j, Φ_j denote the polar radius and polar angle of j-th cutter blade in the follower frame, respectively. To represent the historical lateral trajectory at a given polar angle Φ, the radius function is defined in set form as:

$$P_j(\Phi) = \left\{\rho_j \middle| \Phi_j = \Phi\right\} \tag{15}$$

where $P_j(\Phi)$ is the set of historical radii for j-th cutter blade at angle Φ and generally multi-valued. The calculation formula for the lateral cutting depth of the i-th cutter blade is given by Eq. (16).

$$d_{li} = r - \max_{j=1,2,\dots,N}\left[P_j(\Phi_i)\right],\ \ i = 1, 2, \dots, N \tag{16}$$

This formulation ensures that the lateral depth is governed by the maximum previously generated radius at each angle,

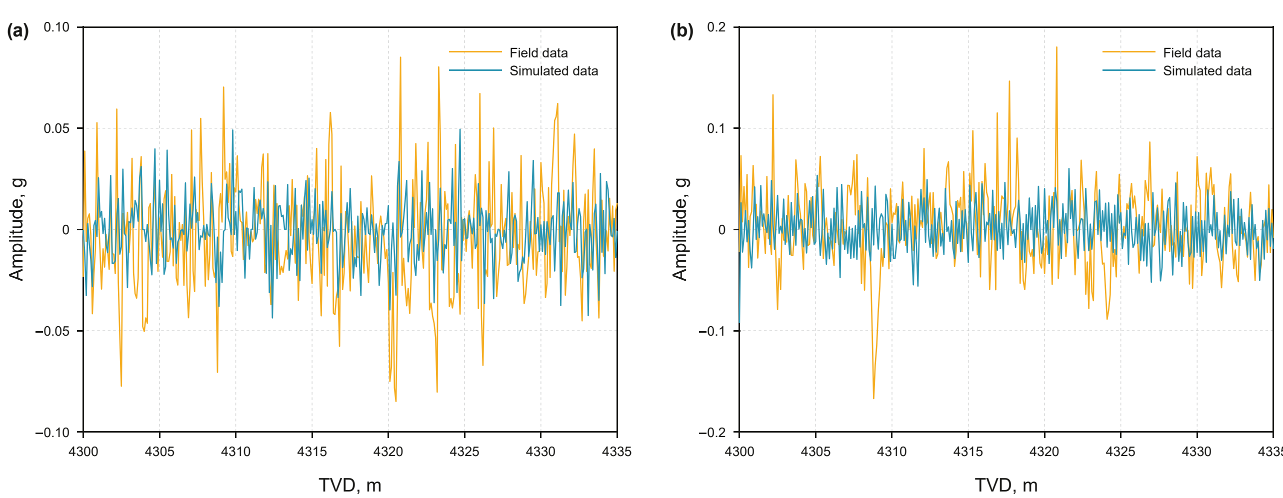

Fig. 6. Time-domain comparison between field measurements and simulation results: (**a**) Lateral acceleration; (**b**) Axial acceleration.

enabling the method to naturally account for regeneration, inter-blade coupling, and arbitrary lateral bit motion. An example is shown in Fig. 4, where the lateral cutting depth of cutter blade 4 is evaluated based on the maximum envelope of the historical radii generated by all blades. In this case, the maximum polar radii $P_2(\Phi_4)$ represents the actual historical lateral cutting displacement, which is generated by the cutting action of cutter blade 2. The lateral cutting depth of cutter blade 4, d_{l4}, is determined by the radius of drill bit r minus the maximum polar radius $P_2(\Phi_4)$.

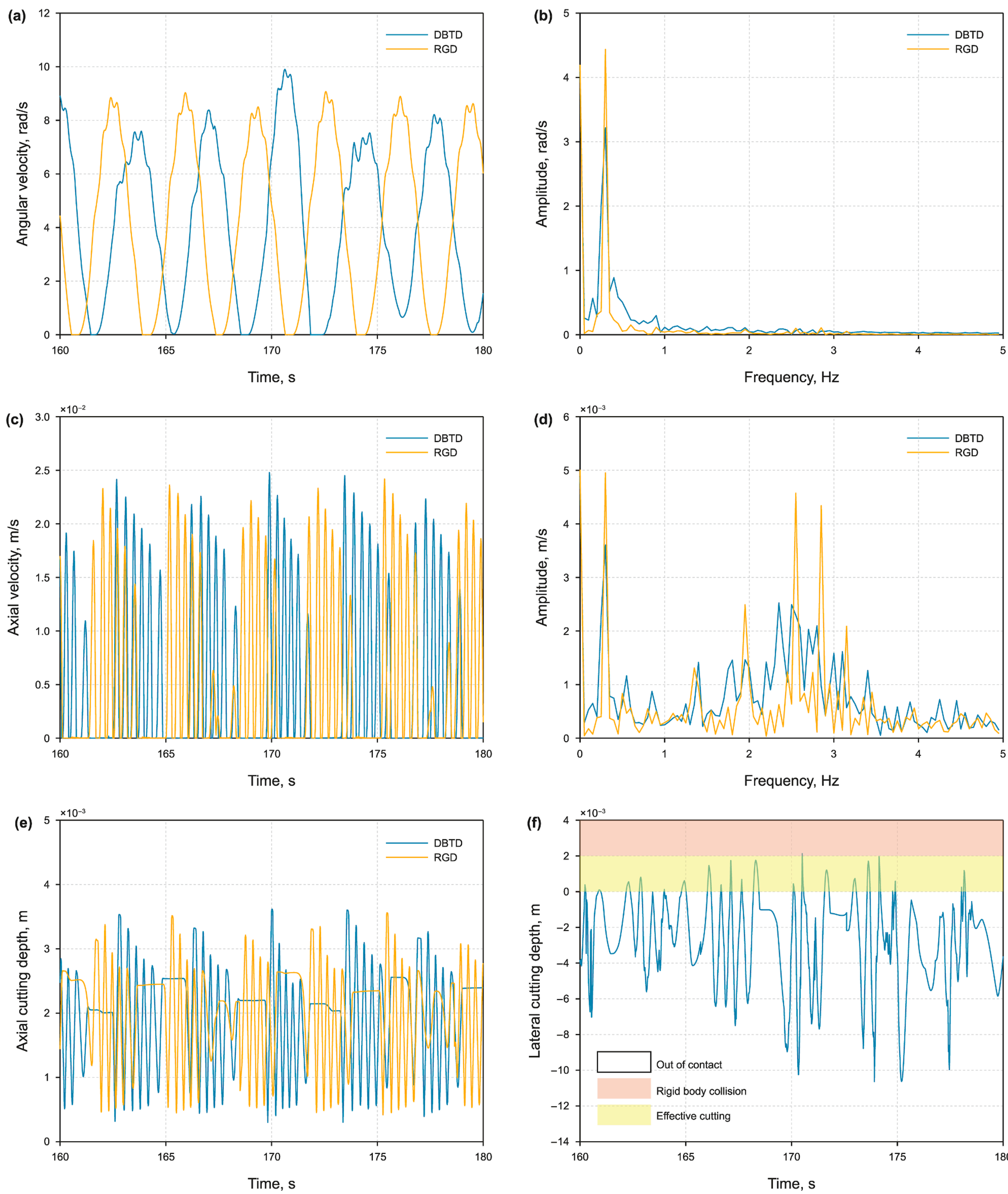

Fig. 7. Comparison between the DBTD and RGD models at a rotational speed of 40 r/min, a downward velocity of 18 m/h, and a WOB of 50 kN. (**a**) Time-domain comparison of angular velocity. (**b**) Frequency-domain comparison of angular velocity. (**c**) Time-domain comparison of axial velocity. (**d**) Frequency-domain comparison of axial velocity. (**e**) Comparison of axial cutting depth. (**f**) Lateral cutting depth in the DBTD model.

2.4. Vibration evaluation index

2.4.1. Evaluation index of stick-slip vibration

The stick-slip index (SSI) is commonly used to evaluate the intensity of stick-slip vibration (Kamel and Yigit, 2014; Long et al., 2023), as follows.

$$\mathrm{SSI}=\frac{\sum_{i}^{n}\left(\dot{\theta}_{i\_\max}-\dot{\theta}_{i\_\min}\right)}{2nw_0},\quad n=\lfloor t_\theta f_\theta \rfloor \tag{17}$$

where n is the number of complete torsional vibration cycles of the drill string that occur within the time window of duration; $\dot{\theta}_{i\_\max}$ is the maximum angular velocity within the i-th torsional velocity period, rad/s; $\dot{\theta}_{i\_\min}$ is the minimum angular velocity within the i-th torsional velocity period, rad/s; t_θ is the total time window duration, s; f_θ is the torsional main frequency, Hz. This n is obtained by multiplying the total time window duration t_θ by the torsional main frequency f_θ, and then taking the integer part (i.e., floor function) of the result.

Although the SSI can characterize the angular velocity fluctuation characteristics and identify the occurrence of stick-slip vibrations, it neglects the amplitude fluctuations of angular velocities in different vibration cycles. These non-stationary amplitude fluctuations can significantly exacerbate the fatigue failure of drill strings. This paper proposes the stick-slip fluctuation index (SSFI) to effectively characterize the amplitude change in stick-slip vibration, as shown in Eq. (18).

$$\mathrm{SSFI}=\frac{n\sqrt{\sum_{i}^{n}\left(\dot{\theta}_{i\_\max}-\frac{1}{n}\sum_{i}^{n}\dot{\theta}_{i\_\max}\right)^{2}}}{\sum_{i}^{n}\dot{\theta}_{i\_\max}},\quad n=\lfloor t_\theta f_\theta \rfloor \tag{18}$$

In this context, a smaller SSFI value indicates a smaller difference between the peak values of the angular velocities in n vibration cycles, which suggests greater amplitude stability of the stick-slip vibration. The characteristic of stick-slip vibration can be more comprehensively depicted with the above two indices.

2.4.2. Evaluation index of lateral vibration

To evaluate the intensity of lateral vibrations in the drill bit, the lateral vibration intensity index (LVII) is proposed based on the lateral contact frequency between the drill bit and the rock within a single torsional vibration cycle, as shown in Eq. (19).

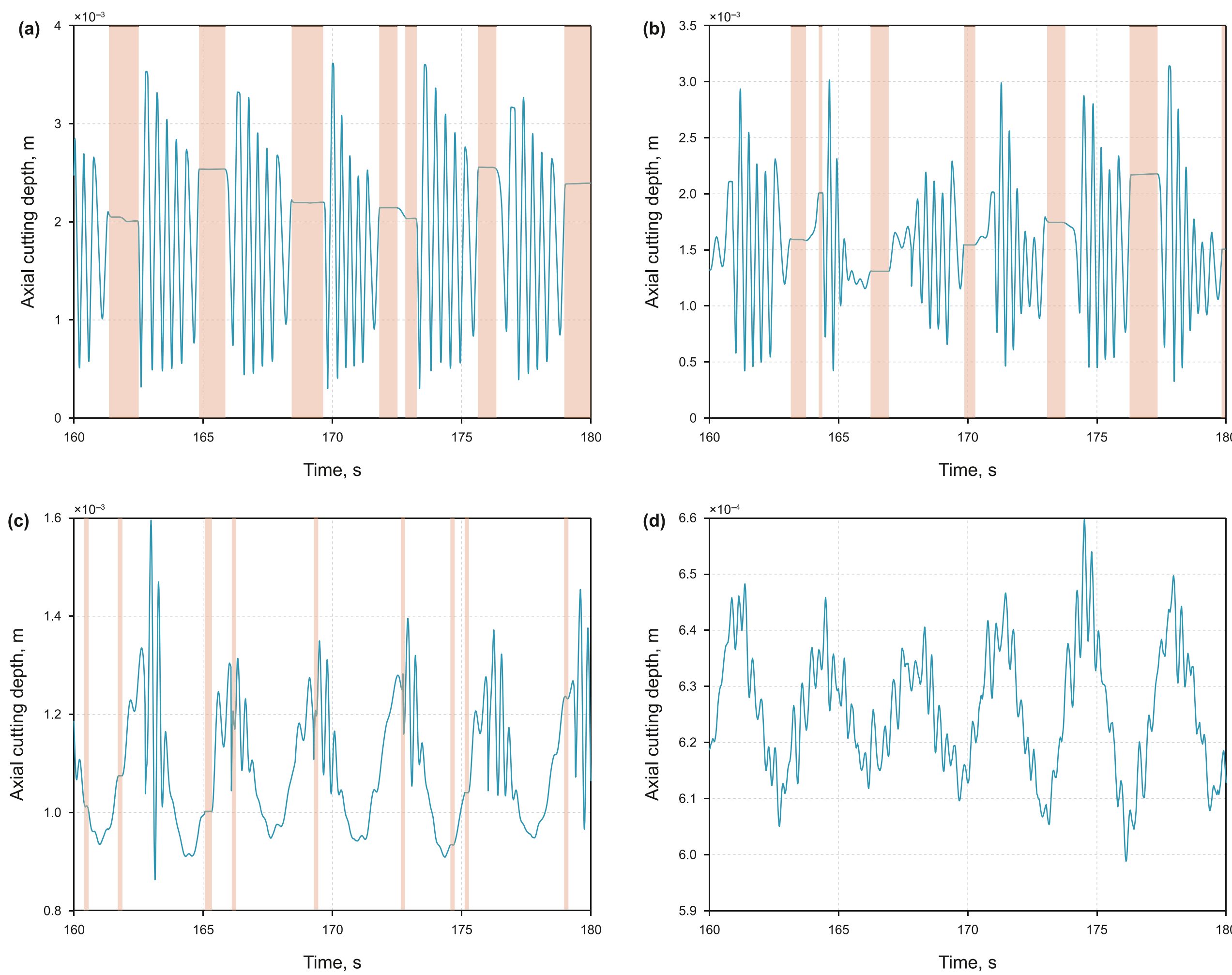

Fig. 8. Axial cutting depth at different rotational speeds. (**a**) 40 r/min. (**b**) 50 r/min. (**c**) 70 r/min. (**d**) 120 r/min.

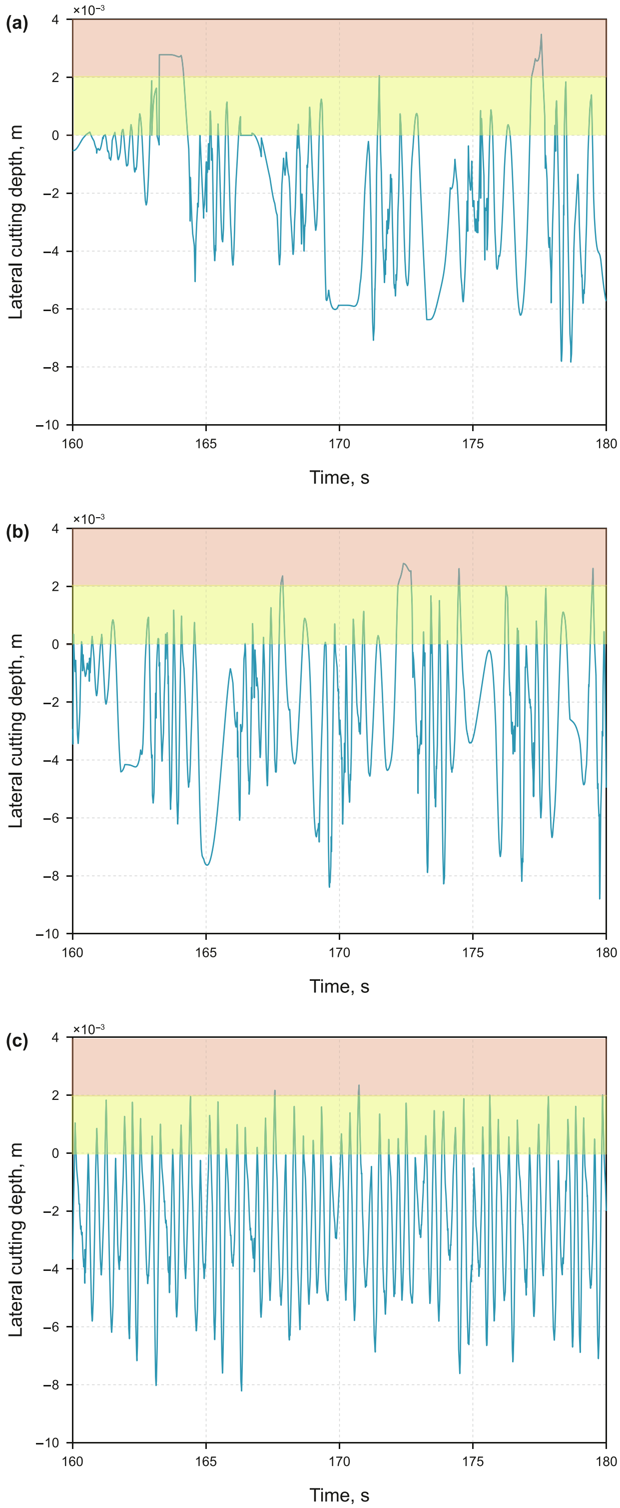

Fig. 9. Lateral cutting depth at different rotational speeds. (**a**) 50 r/min. (**b**) 70 r/min. (**c**) 120 r/min.

$$\mathrm{LVII}=\frac{n_\mathrm{c}}{t_\mathrm{c}f_\theta} \tag{19}$$

where n_c is the number of blade-rock contact events during the contact interval; t_c is the length of the time window, s. The larger LVII value indicates a higher lateral contact frequency between the drill bit and rock within a single torsional vibration cycle, which leads to more pronounced lateral vibrations.

3. Model verification and comparison

3.1. Field data verification

To validate the accuracy and practical applicability of the proposed DBTD model, we selected the 9-1/2″ open-hole section (4035–5079.3 m) of Well BDXX-X-XX, located in the northern fault-step belt of the Baodao Depression, Qiongdongnan Basin, South China Sea. This interval features alternating soft and hard lithologies from the Sanya and Lingshui formations, resulting in heterogeneous, interbedded strata. The drilling tool assembly, from the drill bit to surface, consisted of the following components: a 9-1/2″ Smith SI516 MBPX PDC bit and multiple 6-3/4″ tools, including the ATK, Copilot, OnTrak, ASB, BCPM2, ORD, and CCN. Additional components included a 6-3/4″ topstop sub, a 6-3/4″ hydra-oscillator, a 6-3/4″ reamer stabilizer, a 6-3/4″ junk basket, a 6-3/4″ float valve, a 7″ bridge-plug sub, eight 6-1/2″ drill collars, a 6-1/2″ hydraulic shock absorber, a crossover sub, twelve 5-7/8″ heavy-weight drill pipes, and 5-7/8″ drill pipe (see Fig. 5). During drilling, weight on bit ranged from 2 to 18 tonnes, rotary speed from 60 to 130 rpm, flow rate from 2500 to 2700 L/min, torque from 2 to 20 klb·ft, and pump pressure from 1750 to 2900 psi.

The dynamic simulation was conducted over the interval from 4300 to 4350 m, which is part of the third member of the Lingshui Formation. This interval is characterized by poor drillability, with uniaxial compressive strength typically ranging from 5 to 15 kpsi. The drilling parameters were established as follows: weight on bit was 10 tonnes, rotary speed was 120 rpm, applied torque was 10 klb·ft, mechanical drilling rate was 45 m/h, and the assigned rock strength was 70 MPa. All model inputs, including the bottom-hole assembly geometry, material properties, and formation parameters, were defined based on the actual drill-string components and in-situ conditions for this interval.

As shown in Fig. 6, the comparison of signals for lateral and axial acceleration, between the simulated and measured data, demonstrates excellent overall agreement. It successfully captures the lateral and axial vibration trends and envelope shapes of the drill string. However, the model consistently underpredicts response amplitudes, particularly during localized peak events. This underprediction arises from inherent structural simplifications-namely, the omission of higher-order modal contributions and local resonance phenomena. Furthermore, by neglecting detailed mass-and-flexibility distribution, fluid-structure coupling, and formation heterogeneity, the model incurs some certain degree of error. Nevertheless, despite these simplifications and associated amplitude discrepancies, the model remains highly effective for engineering purposes, as it reliably reproduces the key vibration frequencies and overall dynamic behavior of the drill bit.

3.2. Model comparison

A comparison is made between the DBTD and RGD models, and the values of the relevant parameters are provided in Appendix B. Fig. 7 illustrates the results from the both models at a rotational speed of 40 r/min, a downward velocity of 18 m/h, and a WOB of 50 kN. As shown in Fig. 5(a) and (c), stick-slip vibration occurs in the axial and torsional directions, with the axial velocity rapidly switching between high and low peaks. The magnitude of torsional stick-slip vibration obtained from the DBTD model is more significant than that from the RGD model. As shown in Fig. 5(b) and (d), the same dominant

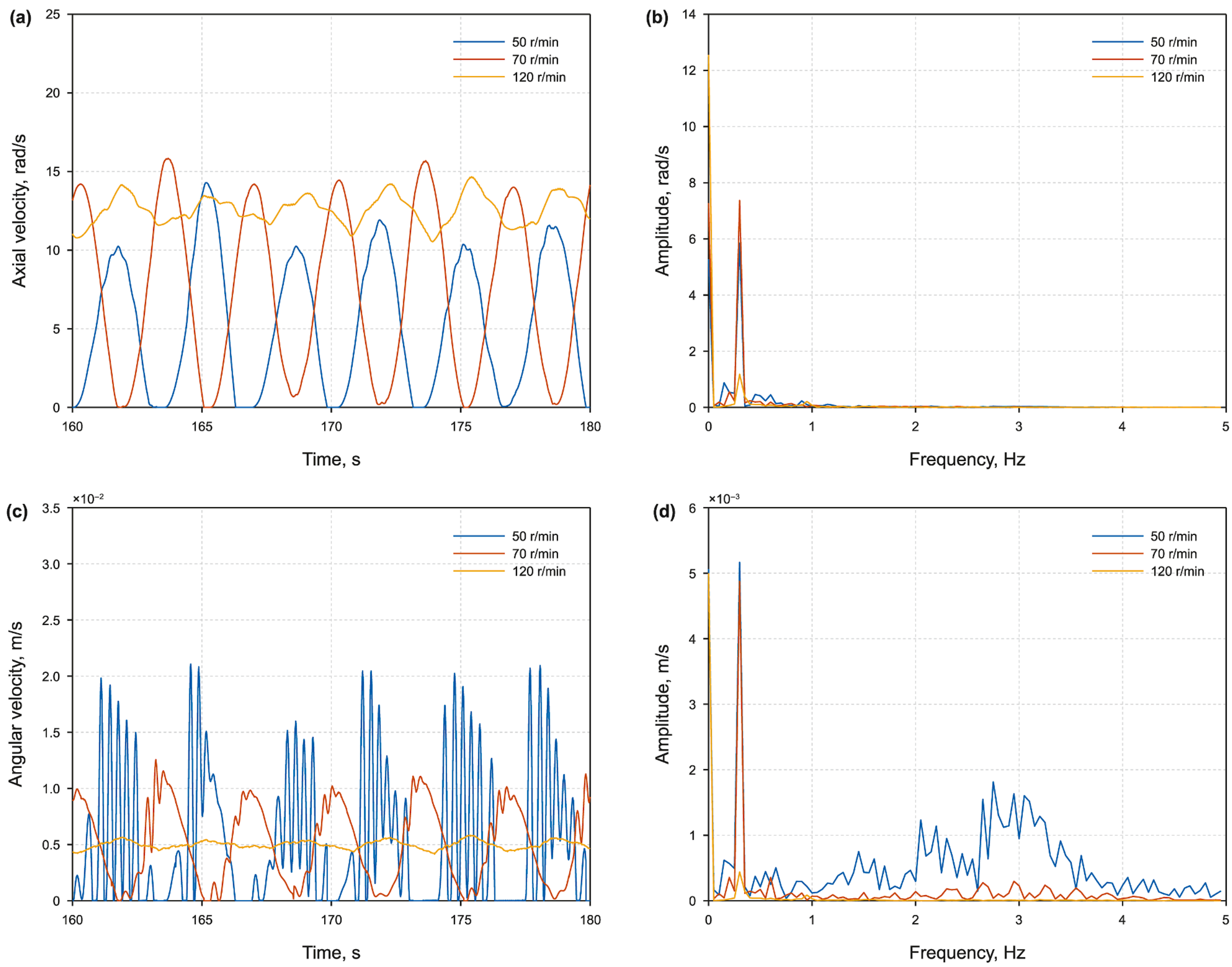

Fig. 10. Comparison of system time-domain and frequency-domain at 50, 70 and 120 r/min rotational speeds. (**a**) Time-domain comparison of angular velocity. (**b**) Frequency-domain comparison of angular velocity. (**c**) Time-domain comparison of axial velocity. (**d**) Frequency-domain comparison of axial velocity.

frequency of 0.299 Hz is in the axial and torsional directions. In the 0–1 Hz range, low-amplitude broadband frequency bands on both sides of the dominant frequency introduce disturbances to the periodic vibration characteristics, leading to amplitude instability. By analyzing Fig. 5(e) and (f), the same characteristics in the axial cutting depth suggest that lateral cutting, rather than axial cutting, is the primary factor contributing to amplitude instability.

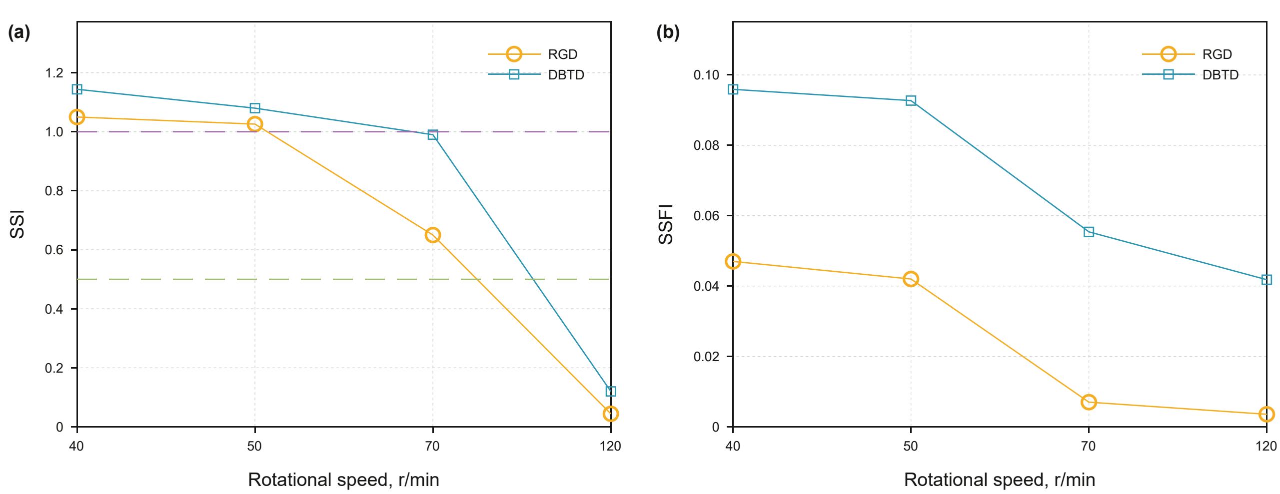

Fig. 11. Comparison between the DBTD model and RGD model. (**a**) Comparison of SSI. (**b**) Comparison of SSFI.

Petroleum Science 23 (2026) 4792–4809

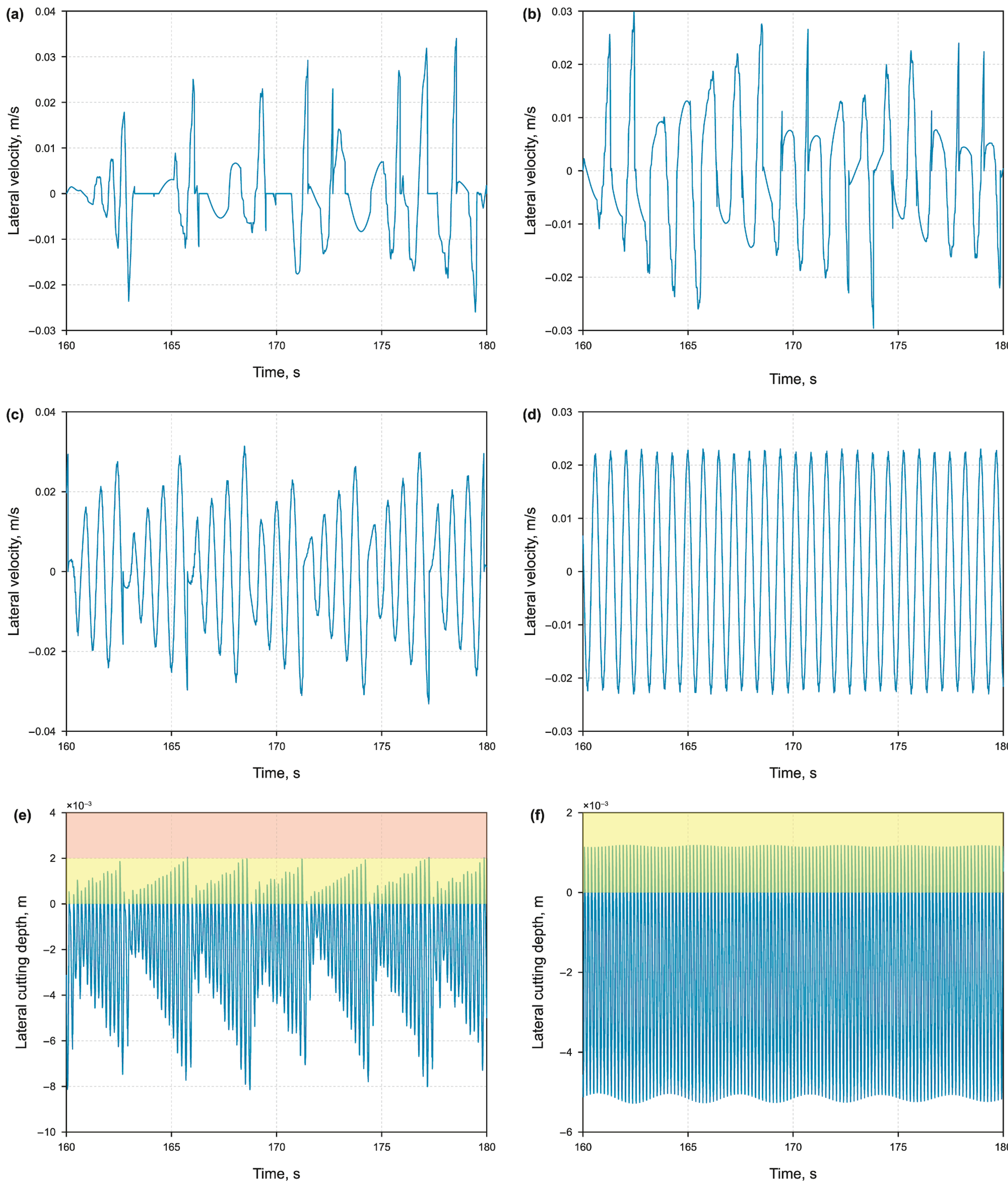

Fig. 12. Lateral motion time-domain analysis at different rotational speeds. (**a**) Lateral time domain at 50 r/min. (**b**) Lateral time domain at 120 r/min. (**c**) Lateral time domain at 240 r/min. (**d**) Lateral time domain at 270 r/min. (**e**) Lateral cutting depth at 240 r/min. (**f**) Lateral cutting depth at 270 r/min.

4. Vibration characteristics analysis

4.1. Analysis of stick-slip vibration evolution

The stick-slip vibration of the drill bit is closely related to the discontinuous rock-breaking motion, which can be explained from the aspect of energy. When the energy on the drill bit is insufficient to sustain the rock-breaking motion, the drill bit enters the sticking phase, and energy accumulates. The rock-breaking motion resumes when the energy exceeds the threshold value, and then the energy is consumed. In the three-dimensional bit-rock interaction model, the axial and lateral cutting depths serve as key indicators of energy consumption during the rock-breaking process. Thus, this section uses rotational speed as the control

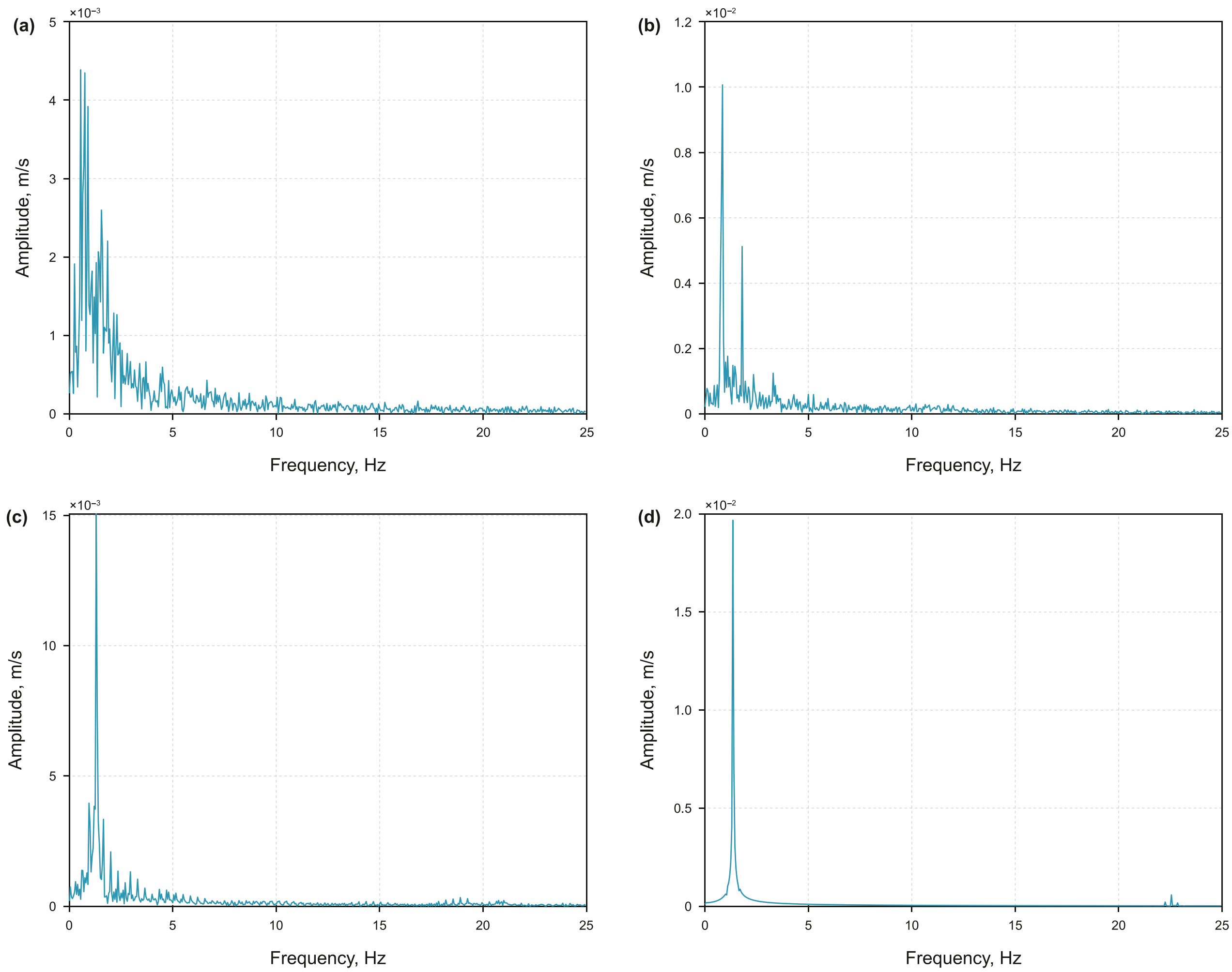

Fig. 13. Lateral frequency domain at different rotational speeds. (**a**) 50 r/min. (**b**) 120 r/min. (**c**) 240 r/min. (**d**) 270 r/min.

variable to systematically investigate the motion characteristics of the drill bit and the variation patterns of axial and lateral cutting depths, to reveal the intrinsic evolution laws of stick-slip vibration.

In the non-vibrating drilling mode, the axial cutting depths of the 4-blade drill bit at an axial speed of 18 m/h and angular velocities of 40, 50, 70, and 120 r/min remain constant at approximately 1.875, 1.5, 1.071, and 0.625 mm, respectively. As shown in Fig. 8, due to the state-dependent time delay caused by torsional vibration and the axial multiple regeneration effect induced by axial vibration, the axial cutting depth exhibits significant fluctuations, with the range of these fluctuations varying according to the intensity of the torsional and axial vibrations. Increasing the rotational speed reduces the axial cutting depth and its corresponding fluctuation, decreases the rock-breaking energy consumption per unit torsional vibration cycle, and consequently narrows the pink region of the axial sticking phase.

The lateral motion of the drill bit is characterized by alternating contact between each cutter blade and the rock. When one cutter blade performs lateral cutting, the resulting asymmetric forces disrupt the lateral force and torque of the drill bit. This disruption affects lateral motion and reduces the amplitude stability. As shown in Figs. 7(f) and 9, the non-periodic fluctuations and the low contact frequency of the lateral cutting depth exacerbate the unstable oscillations of lateral forces, leading to severe lateral rigid-body collisions at low rotational speeds. As the rotational speed increases, the lateral cutting depth transitions to periodic fluctuations, and the lateral cutting frequency increases significantly, reducing the disturbance caused by asymmetric lateral forces.

Subsequently, the evolution of stick-slip vibration is further examined through time-domain and frequency-domain velocity analyses. As shown in Figs. 7 and 10, it is evident that as the rotational speed increases, the system tends to move away from stick-slip vibration. When the rotational speed reaches 70 r/min, the periodic sticking state cannot be sustained, resulting in the system entering an intermittent stick-slip vibration mode. If the rotational speed increases to 120 r/min, the intermittent stick-slip vibration will disappear. This indicates a transitional state, namely intermittent stick-slip vibration, between stick-slip vibration and no stick-slip vibration. At different rotational speeds, no significant amplitude components are observed at the driving fundamental frequency. In contrast, notable amplitudes appear near the torsional natural frequency, indicating that the stick-slip vibration is not externally forced but is self-excited.

To better illustrate the intensity of stick-slip vibration and the stability characteristics of velocity amplitude, this study analyzes both models based on SSI and SSFI. As shown in Fig. 11(a), lateral cutting significantly increases the rotational speed threshold needed for the system to escape stick-slip vibration compared to the RGD model. By combining Figs. 9 and 11(b), lateral cutting significantly reduces amplitude stability. Although increasing the rotational speed mitigates the disturbance caused by lateral cutting on the system vibration, this disturbance is not eliminated entirely.

4.2. Analysis of lateral vibration evolution

The alternating lateral cutting motion of the drill bit results in an imbalance of lateral forces, which induces more pronounced lateral vibrations. This section focuses on using rotational speed as the control variable to further explore the evolution of lateral vibrations from both time-domain and frequency-domain perspectives. Considering the symmetry of lateral motion, only the lateral (x-direction) motion at four representative rotational speeds of 50, 120, 240, and 270 r/min—is selected for comparative analysis.

As shown in Figs. 7 and 12(a), in the stick-slip vibration mode, the lateral motion of the drill bit exhibits a distinct alternating pattern of "collision-cutting-sticking-separation", in which the lateral sticking state is caused by torsional sticking state or lateral rigid-body collisions, disrupting the periodicity of lateral vibration. When the rotational speed increases to 24 r/min, as shown in Fig. 12(c) and (e), the lateral motion exhibits strong periodic characteristics, and disturbances caused by lateral rigid-body collisions prevent the periodic lateral motion from being sustained. When the rotational speed increases to 270 r/min, the lateral motion transitions to an alternating periodic motion characterized by "collision-cutting-separation".

Although the time-domain analysis has provided insights into the evolution process of lateral motion, understanding the dominant factors and mechanisms remains limited. Therefore, the effects of different motion characteristics on lateral vibrations are further explored through frequency-domain analysis. As shown in Fig. 13(a), the lateral motion exhibits a prominent main frequency, with significant frequency amplitudes on both sides and low-amplitude disturbances at high frequencies. This indicates that multiple key factors are influencing the motion. At a rotational speed of 270 r/min, the dominant frequency is found to be 1.35 Hz, which corresponds to the alternating periodic motion of "collision-cutting-separation". In contrast, at 240 r/min, the entire frequency domain exhibits low-amplitude disturbances, suggesting that a pronounced lateral sticking state occurs due to rigid-body collisions.

The above frequency-domain analysis does not distinguish between the effects of lateral sticking state and alternating cutting motion on dynamic behavior. Additionally, the characteristics of alternating cutting motion at low rotational speeds have not yet been revealed. To address this, a time-frequency analysis of the lateral motion is performed using wavelet transform. From Fig. 14(c) and (d), the system demonstrates a stable energy band at 0.0011 kHz, reflecting alternating "collision-cutting-separation" periodic motion. A notable difference is that at 240 r/min, multiple energy bands ranging from 0.0011 to 0.6 kHz are perpendicular to the time axis, reflecting the lateral sticking state caused by the

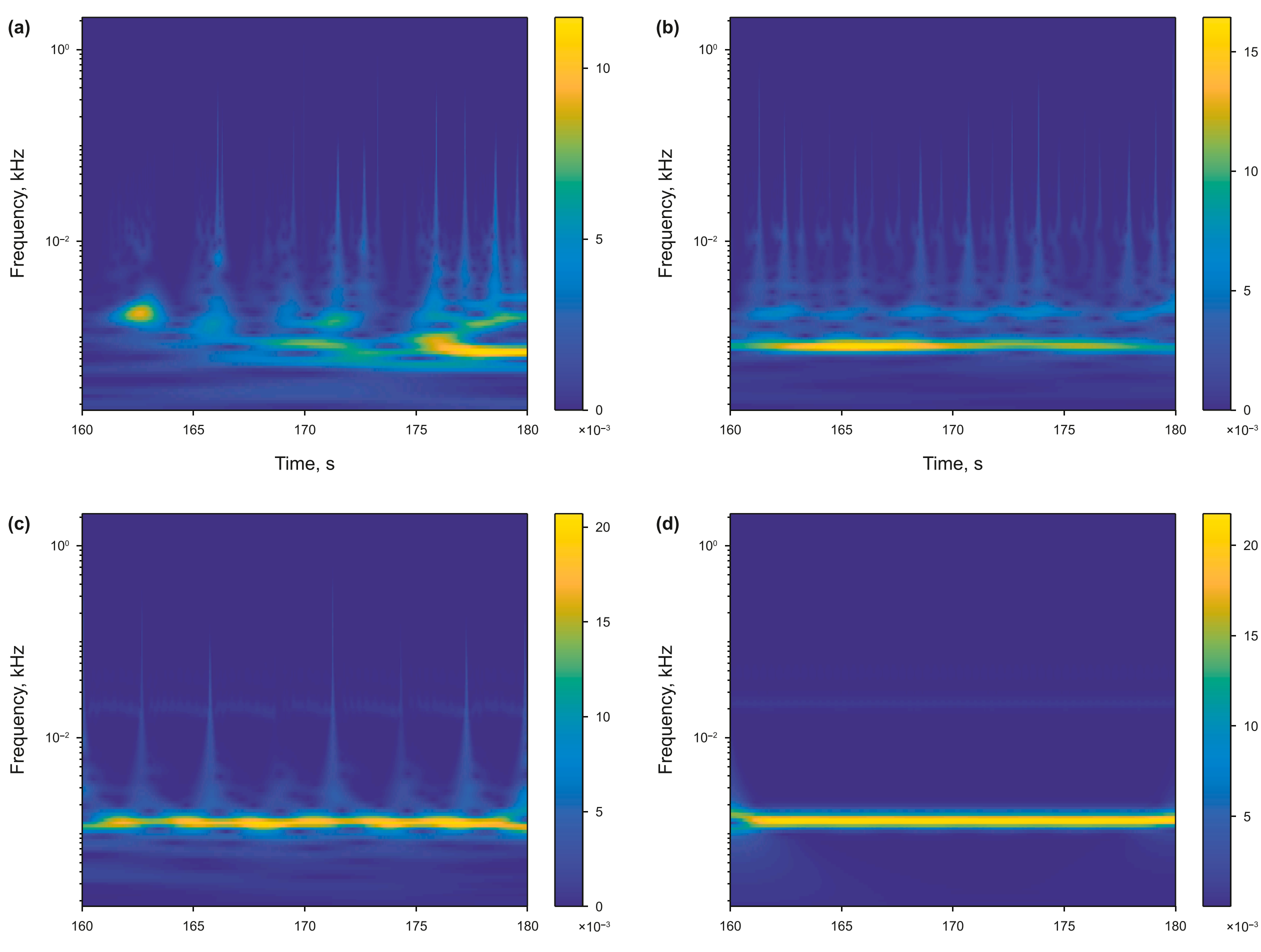

Fig. 14. Time-frequency analysis of lateral motion at different rotational speeds. (**a**) 50 r/min. (**b**) 120 r/min. (**c**) 240 r/min. (**d**) 270 r/min.

rigid body collision. Furthermore, as seen in Fig. 14(a) and (b), the energy bands that are perpendicular to the time axis increase significantly at lower rotational speeds, highlighting a prominent lateral sticking state. When the system undergoes stick-slip vibrations, the frequency-domain range of these perpendicular energy bands expands to 0.0011–1 kHz, indicating that lateral sticking caused by the torsional sticking state is more severe than that due to rigid-body collisions. Additionally, at 50 r/min, the lateral energy spectrum is more uniformly distributed, showcasing a high degree of randomness during the alternating cutting process. Although the lateral vibration comprises both periodic and random components, the random component predominates. As the rotational speed increases, periodicity increasingly governs the lateral motion (exhibiting quasi-periodicity). When the rotational speed reaches 270 r/min, the lateral motion of the drill bit transitions into purely periodic vibration.

The above analysis focuses on the evolution of lateral motion from a dynamic perspective without investigating the whirling characteristics of the drill bit. As shown in Fig. 15, the lateral motion direction is opposite to the rotational velocity. The red arrows represent the instantaneous lateral velocity vectors, with their orientations indicating the motion direction and their lengths indicating the relative speed. The yellow dots indicate the instants when the drill bit experiences rigid-body collision with the borehole wall. The velocity arrows immediately before and after each yellow dot reveals an sudden change in direction, and magnitude caused by the impact. At a rotational speed of 270 r/min, the lateral motion demonstrates backward whirling. However, at rotary speeds of 50, 120, and 240 r/min, the lateral rigid-body impacts or stick-slip vibration prevent the drill bit's lateral motion from sustaining a periodic backward whirling. Extensive numerical simulations have not revealed any critical transition cases for forward whirling. The conditions for forward or backward whirling motion are determined by whether the regeneration force of the drill bit is aligned with or opposite to the direction of rotation (Johnson, 2008). However, when both axial and lateral cutting occur, it is inherently difficult for the drill bit to generate a positive regeneration force that aligns with the rotation direction. Previous studies on the forward whirling of drill bits have considered the coupling effects induced by the whirling of the drill string and simplified the force model of the drill bit, resulting in a positive regeneration force on the drill bit (Gulyayev and Shevchuk, 2016). Nevertheless, in practice, the forward whirling of the drill bit has not been observed (Brett et al., 1989; Li et al.,

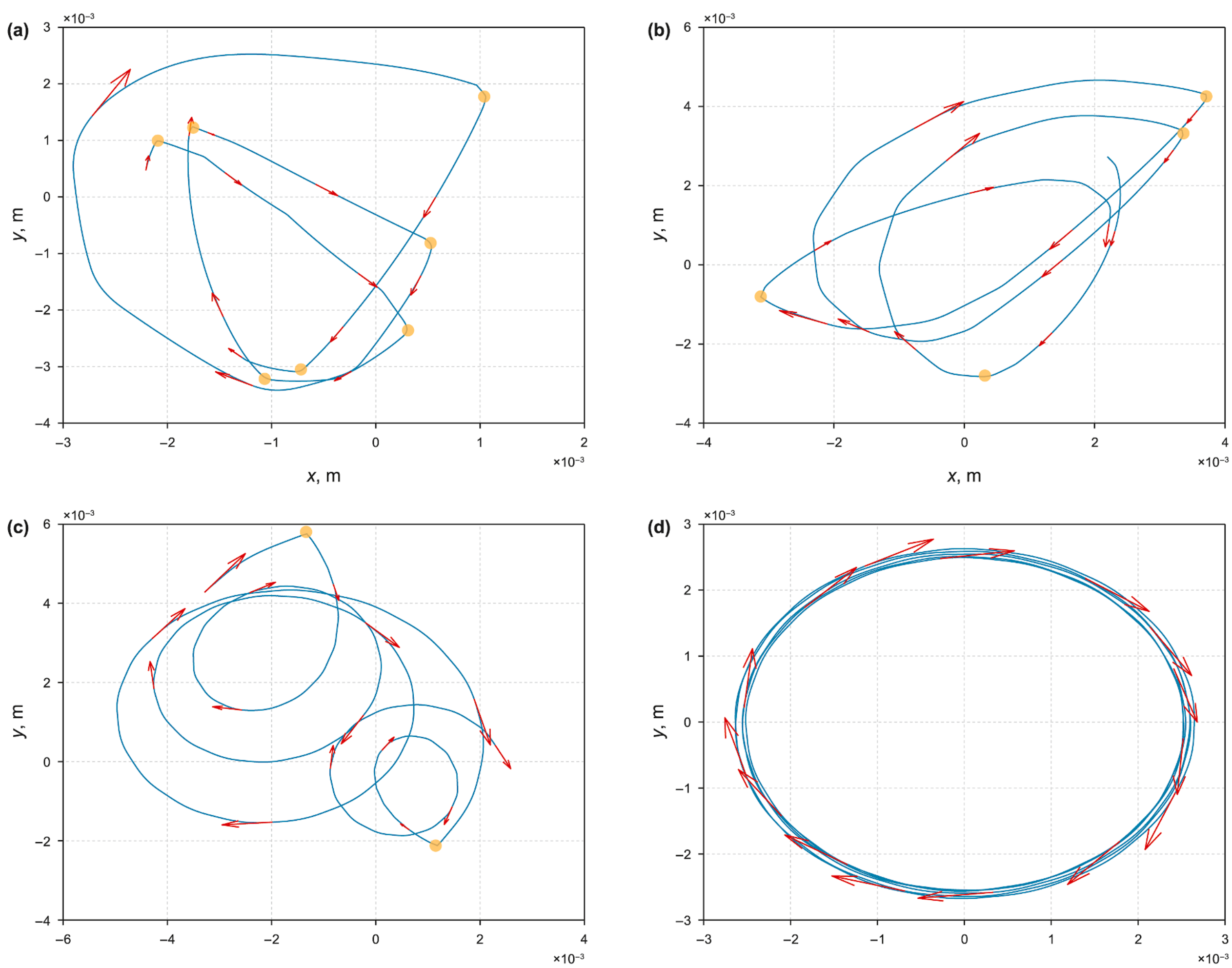

Fig. 15. Lateral motion trajectory at different rotational speeds. (**a**) 50 r/min. (**b**) 120 r/min. (**c**) 240 r/min. (**d**) 270 r/min.

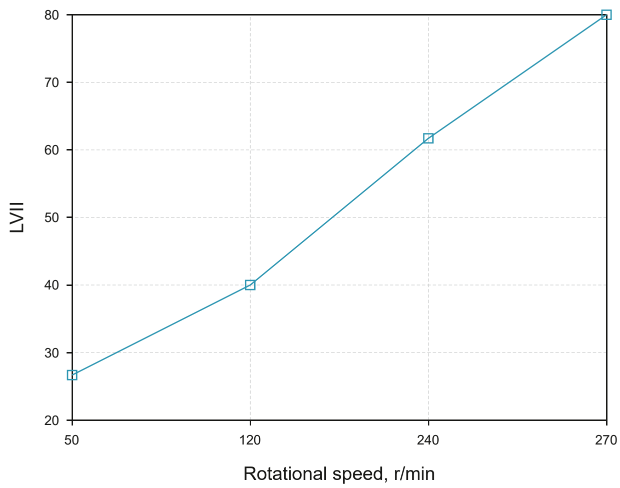

Fig. 16. Lateral vibration intensity evaluation.

2021). Due to the limitations of the DBTD model, it is difficult to investigate the impact of the upper drill string dynamics on the whirling evolution of drill bits.

The above analysis focuses on the lateral vibration of the drill bit from the force perspective but does not evaluate the lateral vibration intensity at different rotational speeds. As the rotational speed increases, the lateral contact frequency per torsional vibration cycle increases, resulting in a corresponding increase in the lateral vibration intensity of the drill bit in Fig. 16. Once the rotational speed reaches a certain threshold, the lateral motion of the drill bit begins to transition into a periodic backward whirl.

5. Conclusions

Based on the above studies, the following conclusions can be drawn.

(1) The lateral alternating cutting action of the drill bit generates asymmetric lateral forces that intensifies stick-slip vibration and improves the critical rotational speed required for the system to escape stick-slip vibration. The amplitude fluctuation induced by lateral cutting persists in the torsional direction even after escaping from stick-slip vibration.
(2) With increasing rotational speed, stick-slip vibration does not directly transition to a non-stick-slip state as previously thought, but rather transitions to intermittent stick-slip vibration and eventually escapes from stick-slip vibration.
(3) At low rotational speeds, the lateral motion of the drill bit follows a "collision-cutting-sticking-separation" pattern characterized by coexisting periodic and random components. As the rotational speed increases, the randomness is significantly reduced until it vanishes, and the lateral motion gradually evolves into a periodic "collision-cutting-separation" motion. Lateral vibration intensity rises with rotational speed, and beyond a critical threshold, the drill bit transitions into backward whirling.
(4) The combined use of the stick-slip index (SSI) and stick-slip fluctuation index (SSFI) provides a comprehensive evaluation of stick-slip vibration severity and quantifies the influence of lateral cutting.

CRediT authorship contribution statement

Jin-Cheng Huang: Writing – review & editing, Writing – original draft, Validation, Data curation, Conceptualization. **Wen-Jun Huang:** Visualization, Validation, Supervision, Funding acquisition. **De-Li Gao:** Visualization, Validation, Supervision, Funding acquisition. **Wen-Tuo Li:** Conceptualization. **Jin-Hui Zhou:** Data curation.

Conflict of interest

The authors declare that they have no known competing financial interests or personal relationships that could have appeared to influence the work reported in this paper.

Acknowledgments

The authors gratefully acknowledge the financial support from the Natural Science Foundation of China (Grant Nos. 2023YFC2810901, 52234002, 52222401, 52394255), the Science Foundation of China University of Petroleum, Beijing (Grant Nos. ZXZX20230083, ZX20250041), and the Science Foundation of the State Key Laboratory of Petroleum Resources and Prospecting (PRP/open-2209).

Appendix A. Geometric limits on axial and lateral cutting depth

In practical drilling with PDC bits, the achievable cutting depth per revolution is constrained by the cutter geometry and by the need to avoid excessively aggressive engagement that can lead to instability, excessive torque and bit damage. Laboratory single-cutter tests and cutter-rock interaction studies therefore typically employ millimetre-scale depths of cut that are small compared with the cutter diameter (Yao et al., 2022; Zhou et al., 2017). To reflect these considerations and to maintain numerical stability in the present dynamic model, explicit geometric limits are introduced on both the axial and lateral cutting depths. Fig. A.1 illustrates the cutting plane in a radial section of the bit and the cone, nose, shoulder and gauge regions of the blade profile, as well as the outward normal of the blade profile at each cutter pocket (Chen et al., 2021b). Along the cone-nose-shoulder part of the profile, the centres of the face cutters lie on this profile, and the outward normal in the cutting plane defines the local cutting direction.

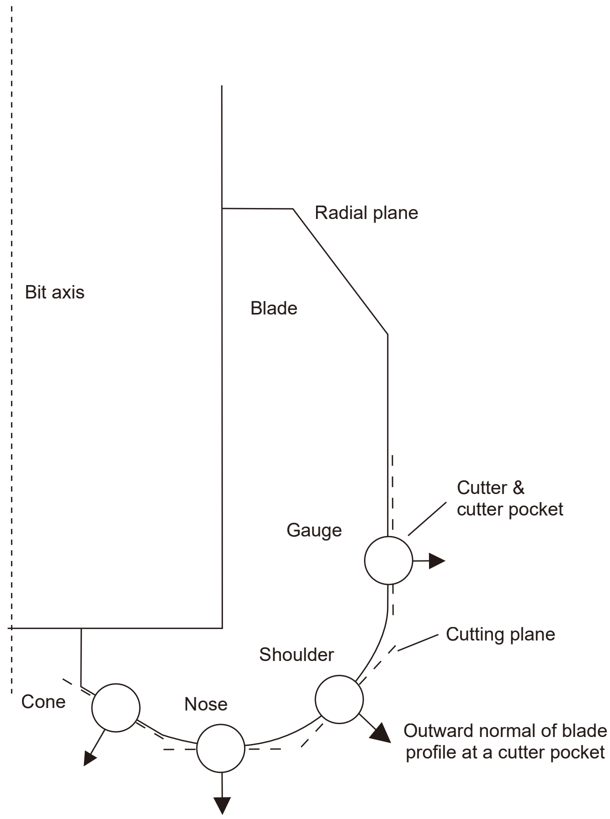

Fig. A.1. Cutting plane and blade profile showing cone, nose, shoulder and gauge regions, cutter pockets and the outward normal of the blade profile at each pocket (Chen et al., 2021b).

In the axial direction, the cutting depth per revolution is limited by the maximum outward exposure of the primary face cutters measured along this local cutting direction. This maximum exposure is specified as a fixed proportion of the face-cutter diameter, so that the corresponding axial depth of cut remains substantially smaller than the cutter size and lies within the millimetre-scale ranges commonly adopted in single-cutter PDC rock-cutting experiments and cutter–rock interaction simulations (Adzis et al., 2018; Liu et al., 2022). In the main model, this maximum exposure defines the axial depth-of-cut limit used for each face cutter.

In the lateral direction, along the gauge section of the blade profile, active gauge cutters and gauge-protection elements engage the borehole wall. For these elements, the relevant measure of engagement is their radial exposure with respect to the bit axis. The lateral depth of cut along the gauge is therefore bounded by the maximum radial exposure of the active gauge cutters and gauge inserts. This gauge exposure is selected as a small fraction of the gauge-cutter diameter, consistent with commercial PDC-bit designs in which gauge-area features such as active gauge structures, penetration-limiting inserts and grit hot-pressed inserts are intended to take only a very small depth of cut with each bit rotation and to limit the penetration of cutters into the borehole wall (Beuershausen, 2002; Dykstra et al., 2002). This maximum gauge exposure defines the lateral depth-of-cut limit adopted for the active gauge cutters in the model.

Appendix B. Parameters and variables

The parameters and model variables used in this study are listed below. The relevant model calculation parameters are referenced from previous research (Liu et al., 2013, 2023).

Parameters	Symbol	Units	Default value
Equivalent mass	m	kg	4.2×10^4
Equivalent moment of inertia	J	kg	184
Equivalent axial stiffness	k_a	N/m	6.2×10^5
Equivalent lateral stiffness	k_b	N/m	2.6×10^5
Equivalent torsional stiffness	k_t	(N·m)/rad	690
Equivalent axial damping	c_a	(N·s)/m	4.9×10^3
Equivalent lateral damping	c_b	(N·s)/m	3.2×10^3
Equivalent torsional damping	c_t	(N·s·m)/rad	8.74
Radius of drill bit	r	mm	108
Height of drill bit	b	mm	100
Intrinsic specific energy of rock	ε	MPa	30
Contact strength of rock	σ	MPa	30
Cutter face inclination	ζ	-	0.6
Friction coefficient for rock-bit interaction	μ	-	0.6
Maximum axial wearflat length of the drill bit	l_{am}	mm	1.2
Maximum lateral wearflat length of the drill bit	l_{lm}	mm	2
Maximum axial cutting depth	d_{ac}	mm	8
Maximum lateral cutting depth	d_{lc}	mm	2
Geometric parameters of drill bit	γ	-	1
Number of cutter blades on drill bit	N	-	4
Wearflat coefficient	κ	-	14
Rotating speed of rotary table or top drive	ω_0	r/min	0–300
Nominal rate of penetration	v_0	m/h	18
Regeneration-order parameter	s	-	12
Weigh on bit	W_0	kN	50

References

Adzis, A.H.A., Abdul-Rani, A.M., Yi, K.Y., et al., 2018. Effect of back rake angle and shape on wear rate of PDC cutter in hard formation. AIP Conf. Proc. 2035 (1). https://doi.org/10.1063/1.5075585.

Ambrus, A., Cayeux, E., Shor, R.J., 2024. Investigation of field scenarios using a 4n degrees of freedom transient torque and drag model. Geoenergy Sci. Eng. 233. https://doi.org/10.1016/j.geoen.2023.212563.

Aribowo, A.G., Wildemans, R., Detournay, E., et al., 2022. Drag bit/rock interface laws for the transition between two layers. Int. J. Rock Mech. Min. Sci. 150. https://doi.org/10.1016/j.ijrmms.2021.104980.

Aribowo, A.G., Wildemans, R., Detournay, E., et al., 2023. Dynamic analysis of a downhole regulator for drilling in interbedded formations. SPE J. 28 (4), 1611–1635. https://doi.org/10.2118/214310-PA.

Bakhtiari-Nejad, F., Hosseinzadeh, A., 2017. Nonlinear dynamic stability analysis of the coupled axial-torsional motion of the rotary drilling considering the effect of axial rigid-body dynamics. Int. J. Non Lin. Mech. 88, 85–96. https://doi.org/10.1016/j.ijnonlinmec.2016.10.011.

Beuershausen, C.C., 2002. Drill bit with selectively-aggressive gage pads. U.S. Patent 6349780B1.

Brett, J.F., Warren, T.M., Behr, S.M., 1989. Bit whirl: A new theory of PDC bit failure. In: Proceedings of SPE Annual Technical Conference and Exhibition. https://doi.org/10.2118/19571-PA.

Cai, M., Mao, D., Li, X., et al., 2023. Downhole vibration characteristics of 3D curved well under drillstring-bit-rock interaction. Int. J. Non Lin. Mech. 154, 104430. https://doi.org/10.1016/j.ijnonlinmec.2023.104430.

Chen, J., Liao, H., Zhang, Y., et al., 2021a. A torsional-axial vibration analysis of drill string endowed with kinematic coupling and stochastic approach. J. Pet. Sci. Eng. 198. https://doi.org/10.1016/j.petrol.2020.108157.

Chen, P., Miska, S., Yu, M., et al., 2021b. Modeling of cutting rock: From PDC cutter to PDC bit—modeling of PDC bit. SPE J. 26 (6), 3465–3487. https://doi.org/10.2118/206725-pa.

Choe, Y.M., Jin, H.S., Kim, G.S., et al., 2022. Axial-torsional mode correlation analysis of a drill string system with non-smooth characteristics. J. Pet. Sci. Eng. 218. https://doi.org/10.1016/j.petrol.2022.110870.

Dehkordi, M.K., Osguei, A.T., Khamoushi, I., et al., 2022. Internal mechanics of anti stick–slip tool. Int. J. Mech. Sci. 221. https://doi.org/10.1016/j.ijmecsci.2022.107188.

Deng, P., Tan, X., Bai, et al., 2024. Influence of blades' shape and cutters' arrangement of PDC drill bit on nonlinear vibration of deep drilling system. J. Sound Vib. 572. https://doi.org/10.1016/j.jsv.2023.118165.

Deng, P., Zhang, A., Fu, K., et al., 2021. Nonlinear vibration of a time-space coupled drill string system based on the surface morphology of rock. J. Sound Vib. 506. https://doi.org/10.1016/j.jsv.2021.116153.

Detournay, E., Defourny, P., 1992. A phenomenological model for the drilling action of drag bits. International journal of rock mechanics and mining sciences & geomechanics abstract 29 (1), 13–23. https://doi.org/10.1016/0148-9062(92)91041-3.

Detournay, E., Richard, T., Shepherd, M., 2008. Drilling response of drag bits: Theory and experiment. Int. J. Rock Mech. Min. Sci. 45 (8), 1347–1360. https://doi.org/10.1016/j.ijrmms.2008.01.010.

Di, Q., Yang, H., Wang, W., et al., 2024. Research advances and development trend of drill string dynamics. Pet. Sci. Bull. 9 (2), 224–239. https://doi.org/10.3969/j.issn.2096-1693.2024.02.017 (in Chinese).

Dykstra, M.W., Heuser, W., Doster, M.L., et al., 2002. Drill bits with reduced exposure of cutters. U.S. Patent 6460631B2.

Faghihi, M.A., Mohammadi, H., Yazdi, E.A., et al., 2024. Distributed model for the drill-string system with multiple regenerative effects in the bit-rock interaction. J. Sound Vib. 571. https://doi.org/10.1016/j.jsv.2023.118120.

Feng, T., Bakshi, S., Gu, Q., et al., 2019. Design optimization of bottom-hole assembly to reduce drilling vibration. J. Pet. Sci. Eng. 179, 921–929. https://doi.org/10.1016/j.petrol.2019.04.107.

Gao, D., Huang, W., 2024. Research and development suggestions on theory and techniques in ultra-deep well engineering. Petroleum Drilling Techniques 52 (2), 1–11. https://doi.org/10.11911/syztjs.2024024 (in Chinese).

Gulyayev, V.I., Shevchuk, L.V., 2016. Drill string bit whirl simulation with the use of frictional and nonholonomic models. J. Vib. Acoust. 138 (1). https://doi.org/10.1115/1.4031985.

Hou, X., Liu, X., Long, X., et al., 2023. Nonlinear axial-torsional vibrations of a drill string with complex delay. J. Dynamics. Control. 21 (8), 55–67. https://doi.org/10.6052/1672-6553-2023-019 (in Chinese).

Johnson, S., 2008. A new method of producing laterally stable PDC drill bits. SPE Drilling & Completion 23 (3), 314–324. https://doi.org/10.2118/98986-PA.

Kamel, J.M., Yigit, A.S., 2014. Modeling and analysis of stick-slip and bit bounce in oil well drillstrings equipped with drag bits. J. Sound Vib. 333 (25), 6885–6899. https://doi.org/10.1016/j.jsv.2014.08.001.

Khulief, Y.A., 2025. Modeling of rotary drillstring vibrations: An overview. Int. J. Struct. Stabil. Dynam., 2630002 https://doi.org/10.1142/S0219455426300028.

Kriesels, P., Keultjes, W., Dumont, P., et al., 1999. Cost savings through an integrated approach to drillstring vibration control. In: Proceedings of SPE/IADC Middle East Drilling Technology Conference and Exhibition. https://doi.org/10.2118/57555-MS.

Kumar, K., Gupta, S.K., Wahi, P., 2024. Rotary drilling dynamics with an asymmetric distribution of cutters on the drill-bit. Nonlinear Dyn. 112 (18), 15857–15882. https://doi.org/10.1007/s11071-024-09865-5.

Li, L.X., Wang, J., Yu, Y.M., et al., 2021. A review of the research and development of high-frequency measurement technologies used for nonlinear dynamics of drillstring. Shock Vib. 2021. https://doi.org/10.1155/2021/8821986.

Li, S., Chen, Z., Li, S., et al., 2024a. Dynamics of resonance impact drilling based on constant depth-of-cut and state-dependent time delay models. J. China Univ. Pet., Ed. Nat. Sci. 48 (1), 124–132. https://doi.org/10.3969/j.issn.1673-5005.2024.01.013 (in Chinese).

Li, X., Gao, H., Guo, X., et al., 2024b. Research progress and prospect in active and passive control of drill string vibration. Nat. Gas. Ind. 44 (6), 98–110. https://doi.org/10.37155/2717-5197-0619-58 (in Chinese).

Li, Y., Xue, Q., Wang, J., et al., 2022. Pattern recognition of stick-slip vibration in combined signals of drillstring vibration. Measurement 204, 112034. https://doi.org/10.1016/j.measurement.2022.112034.

Liu, J., Chen, Y., Liang, S., et al., 2024. Influence of non-newton rheological parameters of drilling fluid on axial-lateral-torsional coupling vibration of rotating drill string. Geoenergy Sci. Eng. 232. https://doi.org/10.1016/j.geoen.2023.212415.

Liu, X., Long, X., Zheng, X., et al., 2020. Spatial-temporal dynamics of a drill string with complex time-delay effects: Bit bounce and stick-slip oscillations. Int. J. Mech. Sci. 170. https://doi.org/10.1016/j.ijmecsci.2019.105338.

Liu, X., Meng, G., Balachandran, B., 2023. Drill-string stability and stress localization: Influence of complex delay effects and dry friction. Int. J. Non Lin. Mech. 157. https://doi.org/10.1016/j.ijnonlinmec.2023.104559.

Liu, X., Vlajic, N., Long, X., et al., 2013. Nonlinear motions of a flexible rotor with a drill bit: Stick-slip and delay effects. Nonlinear Dyn. 72, 61–77. https://doi.org/10.1007/s11071-012-0690-x.

Liu, X., Zhang, Z., Zheng, X., et al., 2021. Mitigation of stick-slip vibrations in drilling systems with tuned top boundary parameters. J. Vib. Acoust. 143 (5). https://doi.org/10.1115/1.4049377.

Liu, X., Zou, D., Chen, Y., et al., 2022. Analysis of PDC cutter cutting-broken conglomerate based on the discrete element method. Energy Sci. Eng. 10 (9), 3580–3591. https://doi.org/10.1002/ese3.1242.

Liu, Y., Gao, D., 2017. A nonlinear dynamic model for characterizing downhole motions of drill-string in a deviated well. J. Nat. Gas Sci. Eng. 38, 466–474. https://doi.org/10.1016/j.jngse.2017.01.006.

Long, W., Kuang, Y.C., Yang, B., et al., 2023. Experimental study on stick-slip vibration characteristics of drillstring-bit-rock coupling system in horizontal well. Arabian J. Sci. Eng. 48 (9), 12555–12567. https://doi.org/10.1007/s13369-023-07802-z.

Luo, J., Liu, J., Li, Q., 2023. Analysis on coupled axial-torsional stick slip vibration behaviors of drill string in deep well. China Pet. Mach 51 (8), 139–147. https://doi.org/10.16082/j.cnki.issn.1001-4578.2023.08.019 (in Chinese).

Richard, T., Germay, C., Detournay, E., 2004. Self-excited stick-slip oscillations of drill bits. C. R. Mec. 332 (8), 619–626. https://doi.org/10.1016/j.crme.2004.01.016.

Richard, T., Germay, C., Detournay, E., 2007. A simplified model to explore the root cause of stick-slip vibrations in drilling systems with drag bits. J. Sound Vib. 305 (3), 432–456. https://doi.org/10.1016/j.jsv.2007.04.015.

Shi, X.L., Huang, W.J., Gao, D.L., 2021. Mechanical behavior of drillstring with drag reduction oscillators and its effects on sliding drilling limits. Pet. Sci. 18 (6), 1689–1697. https://doi.org/10.1016/j.petsci.2021.09.007.

Shi, X., Huang, W., Gao, D., 2023. Mechanical models of drillstrings with drag reduction oscillators and optimal design methods of vibration parameters in horizontal drilling. Geoenergy Sci. Eng. 224. https://doi.org/10.1016/j.geoen.2023.211585.

Tian, K., Detournay, E., 2021. Influence of PDC bit cutter layout on stick-slip vibrations of deep drilling systems. J. Pet. Sci. Eng. 206. https://doi.org/10.1016/j.petrol.2021.109005.

Tian, K., Ganesh, R., Detournay, E., 2020. Influence of bit design on the stability of a rotary drilling system. Nonlinear Dyn. 100 (1), 51–75. https://doi.org/10.1007/s11071-020-05537-2.

Wang, W.C., Yang, H.Y., Luo, D.K., et al., 2025. The analysis of drill string dynamics for extra-deep wells based on successive over-relaxation node iteration method. Pet. Sci. 22 (8), 3293–3303. https://doi.org/10.1016/j.petsci.2025.05.026.

Xiang, C., Fang, P., Li, H., et al., 2023a. Nonlinear dynamics of a drillstring system with PDC bit in curved wells based on the finite element method. Geoenergy Sci. Eng. 230, 212240. https://doi.org/10.1016/j.geoen.2023.212240.

Xiang, C., Fang, P., Li, H., et al., 2023b. Nonlinear dynamics of a drillstring system with PDC bit in curved wells based on the finite element method. Geoenergy Sci. Eng. 230. https://doi.org/10.1016/j.geoen.2023.212240.

Xie, D., Wu, Q., Xi, Y., et al., 2023. Global modelling of nonlinear spatiotemporal dynamics of a drill-string with multiple regenerative effects. Appl. Math. Modell. 114, 114–132. https://doi.org/10.1016/j.apm.2022.09.037.

Yao, J., Liu, B., Zhu, H., 2022. Discrete element study on rock failure mechanism by shaped PDC cutter under formation conditions with in-situ stress and temperature. In: Proceedings of International Geomechanics Symposium. ARMA-IGS-2022-107. https://doi.org/10.56952/igs-2022-107.

Zhang, H., Detournay, E., 2020. An alternative formulation for modeling self-excited oscillations of rotary drilling systems. J. Sound Vib. 474. https://doi.org/10.1016/j.jsv.2020.115241.

Zhang, H., Detournay, E., 2022. A high-dimensional model to study the self-excited oscillations of rotary drilling systems. Commun. Nonlinear Sci. Numer. Simul. 112. https://doi.org/10.1016/j.cnsns.2022.106549.

Zhang, H., Di, Q., Wang, W., et al., 2022. Numerical stability analysis of the rotary drilling system on the basis of state-dependent delay. J. Vib. Shock 41 (22), 233–240+283. https://doi.org/10.13465/j.cnki.jvs.2022.22.028 (in Chinese).

Zhang, H., Tian, K., Detournay, E., 2024a. A high-fidelity model for nonlinear self-excited oscillations in rotary drilling systems. J. Sound Vib. 573. https://doi.org/10.1016/j.jsv.2023.118193.

Zhang, Y., Ashok, P., Chen, D., et al., 2024b. Coupled drillstring dynamics modeling using 3D field-consistent corotational beam elements. Geoenergy Sci. Eng. 233. https://doi.org/10.1016/j.geoen.2023.212424.

Zheng, X., Agarwal, V., Liu, X., et al., 2020. Nonlinear instabilities and control of drill-string stick-slip vibrations with consideration of state-dependent delay. J. Sound Vib. 473. https://doi.org/10.1016/j.jsv.2020.115235.

Zhou, Y., Zhang, W., Gamwo, I., et al., 2017. Mechanical specific energy versus depth of cut in rock cutting and drilling. Int. J. Rock Mech. Min. Sci. 100, 287–297. https://doi.org/10.1016/j.ijrmms.2017.11.004.